Li, M.Y.H., Zhou, M.-F., Williams-Jones, A.E., 2020. Controls on the Dynamics of Rare Earth Elements During Subtropical Hillslope Processes and Formation of Regolith-Hosted Deposits. Economic Geology, 115(5): 1097-1118.

Controls on the Dynamics of Rare Earth Elements During Subtropical Hillslope Processes and Formation of Regolith-Hosted Deposits

Martin Yan Hei Li[1], Mei-Fu Zhou[1*], Anthony E. Williams-Jones[1,2]

1. Department of Earth Sciences, The University of Hong Kong, Pokfulam Road, Hong Kong

2. Department of Earth and Planetary Sciences, McGill University, Montréal, Québec H3A 0E8, Canada

---

*Corresponding author:

Mei-Fu Zhou

Email: mfzhou@hku.hk

Abstract

Sub-tropical weathering of granitic catchments in South China has led to the formation of numerous giant regolith-hosted rare earth element (REE) deposits that are currently responsible for more than 15% of global REE production, and more than 95% if only counting for the heavy REEs (HREE). Low operation cost is a main advantage for exploitation of these deposits. Understanding the controls on the mobilization of the REE and their re-distribution during sub-tropical weathering in these catchments is crucial not only to improving the efficiency of exploration for the deposits in South China but also in other parts of the World. Here, we discuss the controls on REE mobilization in a granitic catchment in southern Jiangxi province, which is the site of the Bankeng LREE prospect. The nature of the primary REE minerals, which include apatite, monazite-(Ce), and subordinate bastnäsite-(Ce), imposes an important control on the behavior of the REE during weathering. Dissolution of these minerals was comparatively slow in the saprock and therefore, REE enrichment in this zone resulted largely from the removal of major elements during the decomposition of albite, K-feldspar, and biotite. Higher in the profile, the primary REE minerals decomposed and released their REEs. The key factors controlling the mobilization and re-distribution of the REEs were the soil pH and redox state. Acidic solutions depleted the surficial soils in the REEs, and transported them to locations, such as the pedolith-saprolite interface, where pH increased due to water-rock interaction, and adsorption on clay minerals efficiently enriched the regolith in the REEs. There was significant Ce accumulation along the saprolite-saprock interface, due to oxidative scavenging of Ce^{3+} by neo-formed Fe-Mn oxyhydroxides and/or precipitation of cerianite [CeO_2]. The location of this accumulation was probably determined by the position of the local groundwater table. Seasonal fluctuations of the groundwater table cause the pH and redox conditions to vary, leading to an irregular REE profile in the saprolite and transition zones.

Along the hillslope, erosion is prevalent at the ridgetop and the intensity decreases towards downslope. Mass balance calculation shows that intensified chemical weathering coupled with the strong erosion at the ridgetop caused the REE enrichment, as the REEs, especially the LREEs, were released from their primary sources and adsorbed on the newly-formed kaolinite from the decomposition of albite, K-feldspar, and biotite. Significant removal of the major minerals also led to apparent enrichment of the REEs. Whereas the HREEs are lost preferentially to the groundwater and transported downslope, enriching the lower part of the weathering crust at footslope in these elements. At the footslope, erosion weakens and chemically depletion due almost entirely to chemical weathering, causing the preferential depletion of the LREEs. In summary, intense erosion facilitates chemical weathering and the REE accumulation and on the other hand, development of a thick ore body would be favored under conditions of weak erosion. Repeated periods of high and low denudation rates caused the gradual development of thick, REE-rich, weathering crusts at the ridgetops to form these economic deposits in sub-tropical South China.

Key words: Rare Earth Elements, REE enrichment, Ce anomaly, redox, sub-tropical weathering, regolith-hosted REE deposits

1. Introduction

The rare earth elements (REEs), comprise the lanthanide group of elements from lanthanum (La) to lutetium (Lu) plus yttrium (Y) and scandium (Sc) and, with the exception of Sc are geochemically important for tracing and understanding a variety of geological processes due to the similarity in their behavior (Henderson, 2013). They have also become economically important because of their unusual properties, which has made them essential elements for a variety of high-technology applications (Goodenough et al., 2018). Currently, more than 15% of the global REE production is from the regolith-hosted deposits (Roskill, 2011). More importantly, however, these deposits supply more than 95%, of the global HREE demand (García et al., 2017). Regolith-hosted REE deposits form by progressive REE accumulation and enrichment in soils during the weathering of a variety of rock types, including granites, felsic volcanic rocks, and schists, and in the case of the HREE, highly fractionated alkaline granites (Sanematsu and Watanabe, 2016; Li et al., 2017). The occurrence of these deposits is largely confined to the sub-tropical environment of South China, northern Vietnam, Myanmar, Madagascar, Malawi, and Brazil (Li et al., 2017).

It has been known since the late 1970's that the REEs are mobile during weathering (Nesbitt, 1979), and since then there have been numerous investigations of the behavior of the REE during weathering (e.g. Duddy, 1980; Braun et al., 1993; Gouveia et al., 1993; Mongelli, 1993; Condie et al., 1995; Nesbitt and Markovics, 1997; Aubert et al., 2001; Ma et al., 2007; Jin et al., 2010; Yusoff et al., 2013; Jin et al., 2017). As a result of these studies, it has been established that the mobility of REEs during weathering is controlled by pH, redox conditions, their aqueous complexation, the primary REE mineralogy, the precipitation of secondary REE minerals and the adsorption of the REEs by clay minerals, Fe-Mn oxyhydroxides, and organic substances in soils (e.g. Cantrell and Byrne, 1987; Banfield and Eggleton, 1989; Braun et al., 1990; Koeppenkastrop and De Carlo, 1992; Braun et al., 1998; Aubert et al., 2001; Pourret et

al., 2007; Laveuf and Cornu, 2009; Yusoff et al., 2013; Su et al., 2017; Braun et al., 2018; Lara et al., 2018; Li et al., 2019).

In tropical environments, strong leaching of the REEs takes place in the uppermost nodular and ferruginous duricrust horizon of the soil profile, whereas accumulation of the REEs occurs as secondary REE minerals in the lower mottled clay horizon and saprolite (Braun et al., 1993; Braun et al., 1998; Ma et al., 2007; Berger et al., 2014; Lara et al., 2018) or through adsorption on clay minerals (Galán et al., 2007; Sanematsu et al., 2013; Yusoff et al., 2013). Usually, the light REEs (LREEs) are preferentially accumulated in the soil profile, whereas heavy REEs (HREEs) are lost to groundwater and rivers (Nesbitt, 1979; Elderfield et al., 1990; Braun et al., 1998; Galán et al., 2007; Laveuf and Cornu, 2009; Braun et al., 2012; Yusoff et al., 2013; Babechuk et al., 2014; da Silva et al., 2017) leading to LREE-HREE fractionation (Nesbitt, 1979; Duddy, 1980; Braun et al., 1990; Braun et al., 1993; Sanematsu et al., 2013; Yusoff et al., 2013). Cerium also fractionates from the other LREEs, producing Ce anomalies in soil profiles (Braun et al., 1990; Braun et al., 1998; Ma et al., 2007; Laveuf and Cornu, 2009; Yusoff et al., 2013; Berger et al., 2014). There are multiple reasons for this, including oxidation and/or scavenging of Ce by Fe or Mn oxides and precipitation of cerianite-(Ce) (Duzgoren-Aydin and Aydin, 2009; Sanematsu et al., 2013; Berger et al., 2014). The cause of the oxidation is usually the development of oxic fronts due to seasonal fluctuations in the groundwater table (Braun et al., 1990; Braun et al., 1998; Ma et al., 2007; Babechuk et al., 2014; Lara et al., 2018).

In addition to climate, weathering and denudation also vary with the evolution of the hillslope (Thomas, 1994; Taylor and Eggleton, 2001; Schaetzl and Anderson, 2005; Schaetzl, 2013), which, in turn, controls REE depletion and enrichment. In tropical and sub-tropical environments, a convex-concave hillslope landscape, with a relief generally less than 100 m and a slope of 20 - 25º, is commonly produced by the coupled effect of denudation and weathering (Thomas, 1994; Migoń, 2009, 2013). Variations in the slope convexity and

111 concavity lead to differences in the intensity of slope processes, such as runoff erosion, creep,
112 and landslide. If denudation is intense in the upslope environment, downslope transport of the
113 REE can be significant and is associated with surface runoff, and sub-surface throughflow and
114 groundwater flow during hillslope evolution. These processes increase the mobility and re-
115 distribution of the REEs across a catchment (Schaetzl and Anderson, 2005).

116 Despite the importance of sub-tropical weathering to REE accumulation and ore
117 formation in soils, the behavior of the REE during sub-tropical weathering is poorly understood.
118 Moreover, previous studies of regolith-hosted REE deposits have focused mainly on vertical
119 mobilization and re-distribution of the REEs (e.g. Wu et al., 1990; Bao and Zhao, 2008;
120 Murakami and Ishihara, 2008; Sanematsu et al., 2013; Foley et al., 2015; Sanematsu et al.,
121 2016; Li et al., 2019), whereas the variation along hillslopes and the role of geomorphological
122 processes has been largely neglected. Nonetheless, geomorphology is one major control on
123 elemental re-distribution during weathering (Taylor and Eggleton, 2001). Hillslope processes,
124 such as erosion, infiltration, throughflow, and baseflow, could mobilize and transport the REEs
125 causing spatial variations in REE concentration across the catchment. Preservation of the
126 deposits is also controlled by these hillslope processes. Understanding the geomorphological
127 control is essential to ensure the discovery of new regolith-hosted REE deposits, not only in
128 South China but also in similar environments elsewhere. In this study, we investigate the
129 geomorphological processes in a sub-tropical granitic catchment, in which the Bankeng LREE
130 prospect situates, and the control on REE mobilization and re-distribution across the catchment.
131 Here, we relate different geomorphological processes and the mass balance at an ore-bearing
132 hillslope to explain the favorable geomorphological condition to form this kind of deposits.
133

134 **2. Site description**

The study area is a catchment located in southern Jiangxi province, South China where there is a subtropical monsoon climate, an annual rainfall of 1,200 - 1,900 mm and the average temperature is 18 - 21°C (Zhang, 1989; Huang et al., 2013). There are wet and dry seasons , with 47% of the annual precipitation falling within the wet season (Zhang, 1989). In the catchment, the Bankeng LREE prospect is hosted (Fig. 1), although the exploration is still undergoing and there has been no mining activity in the study area. In addition, the study area is adjacent to the world-class Zudong regolith-hosted HREE deposits (Fig. 1) and the prospect area is also designated as a potential exploration target for economic HREE mineralization.

Regionally, the catchment sits on a gently undulating landform with an elevation varying between 350 and 400 m above sea level (Fig. 1). The hillslopes consist mainly of a convex upslope segment and a concave footslope segment. The relief is gentle and the slope gradient varies between ~15 - 20°. Weathering crusts up to 60 m thick are developed in the region (Li et al., 2017), although in the catchment investigated, the thickness of the crust varies between 1 and ~10 m; it increases gradually from the ridgetops to the footslopes (Fig. 1). In profile, the weathering crust is clearly zoned from a humic layer at the top downward through a pedolith zone, a saprolite zone, a saprock zone and a bedrock composed of alkaline granite (Fig. 2).

The catchment is covered by sub-tropical forests (Liu and Wu, 2017). Trees (pinus massoniana, cuninghamia lanceolate, pterocarya stenoptera, rhus chinensis) dominate the valleys, whereas the ridges are covered by both trees and shrubs (miscanthus floridulus). The local groundwater is neutral to slightly alkaline in nature with pH values varying between 7 to 8, and its total REE concentration is about 4 ppb, mainly the HREEs (Li et al., 2019). There is continuous seepage in the transition zone between the saprolite and saprock of the footslope, suggesting that this zone coincides with the groundwater table.

3. Sampling strategy and analytical methods

3.1 Augered soil coring, diamond drill coring, and petrographic observation

Samples of different parts of the soil profile were collected using a 2-in. diameter soil auger to a depth varying from 0 to 4.5 m. Three soil profiles were sampled, i.e., at the ridgetop, upslope and footslope, the locations and sampling sites of which are shown in Figure 1. In the case of the footslope profile, the saprock and bedrock were sampled with a rotary drill. The core recovery was generally greater than 90%. Petrographic observations were made using optical microscopy and a scanning electron microscope, equipped with an Oxford INCAx-sight energy-dispersive spectrometer at the Electron Microscope Unit (EMU), the University of Hong Kong.

3.2 Quantitative X-ray diffraction (XRD) analysis

The major minerals were identified and their abundances determined using quantitative X-ray diffraction (XRD) analyses. Samples were ground to a fine powder using an agate mortar and pestle and analyzed at the China University of Geosciences (Wuhan) with a D8 Focus Bruker powder X-ray diffractometer. Each sample was X-rayed with non-monochromated Cu Kα radiation (40 kV, 40 mA) from 2º to 70º 2θ at a scanning speed of 2º per minute. The diffractograms were analyzed using JADE 6.5 software and the proportions of the different minerals determined through a Rietveld refinement.

3.3 Measurements of soil pH and total organic carbon content (TOC)

The pH of the samples was measured using the method of Ma et al. (2007). Ten grams of deionized water were equilibrated with five grams of sample powder for eight hours. The supernatant liquids were collected after filtration and their pH values measured using an Orion 210A+ acidity meter with a precision better than 0.05.

The total organic carbon contents were determined by ALS Chemex (Guangzhou) Co. Ltd. Accurately weighed samples were digested with dilute hydrochloric acid and the solutions subsequently filtered through a porous Leco crucible for organic carbon separation. The residues were rinsed with deionized water and dried and then subjected to direct combustion in a high frequency Leco induction furnace in a stream of oxygen before measurement of the infrared adsorption. The detection limit was 0.01%.

3.4 Bulk major and trace element analysis

Major element abundances were determined using wavelength-dispersive X-ray fluorescence spectrometry (WD-XRFS) on fused glass beads at the Department of Earth Sciences, the University of Hong Kong. Three grams of sample were weighed and heated at 105ºC and 900ºC for three hours at each temperature to determine the loss of ignition (LOI). The combusted samples were then fused with lithium tetraborate in a 1:10 ratio to prepare glass beads for analysis. The analysis was undertaken with a Axio^{mAX}-Advanced XRFS which provided for an analytical accuracy and precision of <0.5% for major element oxides.

Trace element contents were analyzed at the State Key Laboratory of Ore Deposit Geochemistry, Institute of Geochemistry, Chinese Academy of Sciences, Guiyang. Approximately 0.05 g of sample powder was digested with a mixture of HNO_3 and HF in a closed Telfon bomb, and heated in an oven at 190ºC for 40 hours. The digested samples were dried at 200ºC and re-digested with HNO_3 at 140ºC for another eight hours. Rhodium standard solution was used as an internal standard. Pure elemental standards for external calibration with OU-1 and AMH-1 as reference materials were also employed. The analyses were carried out with a VG PQ Excell ICP-MS to an accuracy of better than 5% (Qi et al., 2000).

3.5 Sequential extraction experiment

A three-step sequential extraction following the method of Li et al. (2019) was used to evaluate the elemental distribution in the regolith samples The targets of the extraction were the exchangeable clay-adsorbed component (Step 1), the Fe-Mn oxyhydroxide-adsorbed component (Step 2), and the organic matter-bound component (Step 3). The solutions used in the extractions for Steps 1, 2, and 3 were 0.5 M ammonium sulfate (adjusted to pH = 4 with H_2SO_4), 0.5 M ammonium hydroxylammonium chloride (adjusted to pH = 2 with HNO_3) and 0.1 M sodium pyrophosphate, respectively. Extractions were performed by adding 40-mL of the extraction solution to 1 g of powdered sample and mechanically shaking for 16 h at room temperature. The supernatant solution was obtained by centrifuging at 3,000 rpm for 20 min and filtering using a cellulose acetate-type membrane filter ($\varphi = 0.22\mu m$). The membrane filter was rinsed repeatedly with 50 mL of Milli-Q double deionized water and the filtered solution acidified to 5% HNO_3 equivalent. A rhodium standard solution was added as an internal standard for subsequent analysis.

The analysis was carried out with an Agilent 7700 ICP-MS at the Water Analysis Laboratory, the Hong Kong Polytechnic University and an Agilent 7900 ICP-MS at the University of Hong Kong. Calibration lines were constructed with multi-element standard solutions MISA-01-1 and -04-1 (AccuStandard). Detection limits of individual elements were determined using blank solutions. The accuracy of the analyses was determined to be <10%.

4. Results

4.1 Petrography and weathering sequence

The catchment considered in this study is underlain by medium- to coarse-grained alkaline granite composed of quartz, K-feldspar, albite, biotite and chlorite, accessory zircon, apatite, monazite-(Ce), thorite, xenotime(Y), magnetite, ilmenite, fergusonite-(Y), and columbite-(Fe). Quantitatively, this rock comprises about 30 wt.% each of quartz, K-feldspar

and albite with the remaining ~10 wt.% consisting of biotite and chlorite (Table S1). Myrmekite, representing an intergrowth of quartz and K-feldspar, is common (Fig. 3a). There is also evidence that the granite was subjected to late magmatic or post-magmatic metasomatism, which formed a variety of secondary REE-bearing minerals, including monazite-(Ce), bastnäsite-(Ce), and fluorite. Rare earth element mobilization and re-distribution was intense during this metasomatism, as shown by the observation that primary apatite was replaced by monazite-(Ce) (Fig. 3b), that monazite-(Ce) occurs as irregularly-shaped grains (Fig. 3c and d), that bastnäsite-(Ce) is abundant (Fig. 3e), and that primary fergusonite grains were altered along their rims (Fig. 3f).

The saprock generally resembles the bedrock, preserving most of the primary mineralogy and granitic texture of the bedrock, although the primary minerals, especially the feldspars and biotite, have been partially replaced, (preferentially along cleavages), the former to kaolinite and halloysite (Fig. 4a), and the latter to vermiculite, and minor smectite (Fig. 2). The weathering intensity is largely controlled by the joint density, with strong staining and decoloring of the saprock being evident in the well-jointed intervals (Fig. 2). This unit transitions up into the saprolite, which is light brown to pale yellow in color and largely preserves the relict granitic texture (Fig. 2), although most of the albite has been replaced by kaolinite and halloysite. The kaolinite mostly occurs as micro-crystalline flakes of a few μm across while the halloysite as <3 μm long tubes (Fig. 4b). Chlorite and biotite also weathered to form vermiculite, which gradually decomposed to form kaolinite (Fig. 4c). Smectite occurs in a minor amount, usually as aggregates of wavy flakes on surface of biotite grains (Fig. 4d). In the overlying pedolith, the relict granitic texture has been destroyed with albite entirely weathered and K-feldspar partially so, both to kaolinite and halloysite (Fig. 2). Both kaolinite and halloysite in this zone could be of larger sizes and higher crystallinity. Vermicular kaolinite "booklet" with size >5 μm commonly occurs (Fig. 4e) whereas halloysite mostly occurs as

euhedral, ~5 μm long tubes (Fig. 4f). Abundant neo-formed goethite and anatase precipitated in this zone. Quartz was largely unaffected and accumulates as a residual phase.

The weathering profile contains a variety of relict grains of parental REE minerals, including monazite-(Ce), xenotime-(Y) and thorite that have been partially dissolved, as shown by the occurrence of corroded grain boundaries (Fig. 5a - c) and crosscut by supergene goethite veinlet (Fig. 5c). Zircon is likely more resistant and weathering is restricted to physically abrasion rounding the shape of grain (Fig. 5d) Other REE-bearing minerals of the parent granite, i.e., apatite, bastnäsite-(Ce), and fluorite, are not observed in the saprolite and pedolith, suggesting that they have completely decomposed. Supergene REE minerals are also present in the profile, dominantly rhabdophane-(Ce) and cerianite-(Ce). Irregularly-shaped, inclusion- and fracture-free supergene rhabdophane-(Ce) is spatially associated with partially decomposed primary grains of apatite, monazite-(Ce) and xenotime-(Y) (Fig. 5e). Cerianite-(Ce) occurs as μm-sized, doughnut-shaped grains (Fig. 5f), mainly in the pedolith zone.

4.2 Bulk mineralogical variation

In the footslope profile, the proportions of both quartz and K-feldspar increase from ~30 wt.% in the parent granite to ~35 wt.% in the saprock (Fig. 6). However, that of albite decreases from ~30 wt.% in the parent granite to ~15 wt.% in the saprock. Minor kaolinite, ~2 wt.% is observed (a product of weathering). The proportion of biotite and chlorite varies between 5 and 10 wt.%. In the saprolite, the proportions of both quartz and K-feldspar increase to ~40 wt.% and that of albite drops abruptly to ~2 wt.% (Fig. 6). The proportion of kaolinite rises to 7 wt.% on average. In the pedolith, the proportion of quartz reaches more than 50 wt.%. That of K-feldspar decreases to ~20 wt.% and albite is absent. The proportion of kaolinite rises to ~10 wt.% and the proportion of biotite and chlorite is consistently ~10 wt.% in both the saprolite and pedolith zones.

In the upslope profile, the proportion of quartz varies between 50 and 80 wt.% and, in general, increases gradually from the saprolite to the pedolith zone (Fig. 7a). The proportion of K-feldspar fluctuates between ~10 to 20 wt.%. The kaolinite abundance ranges from 10 – 40 wt.%, varies inversely with the proportion of K-feldspar and is highest in the lower pedolith zone. The proportions of biotite and chlorite generally increase from ~5 wt.% in the saprolite zone to up to 15 wt.% in the pedolith zone.

In the ridgetop profile, the variation in the proportions of the different major minerals is relatively small compared to that in the other two profiles (Fig. 7b). The abundance of quartz decreases slightly from 65 to 55 wt.% with decreasig depth in the saprolite zone but increases sharply to 60 wt.% at the pedolith-saprolite interface, and then gradually decreases towards the surface. In contrast, the proportion of K-feldspar decreases from ~15 wt.% in the saprolite zone to 10 wt.% at the pedolith-saprolite interface, but rises slightly in the pedolith zone. The abundance of biotite and chlorite is relatively consistent of ~10 – 15 wt.%. The abundance of kaolinite is consistently between ~20 – 25 wt.%.

4.2 Bulk geochemical variation

4.2.1 Parent granite

The parent granite has a SiO_2 content of ~78 wt.%, an Al_2O_3 content of ~12 wt.% and an alkali content of >8 wt.% (Table S2). The Fe_2O_3, MgO and TiO_2 contents are comparatively low, 1.50, 0.14 and 0.17 wt.% on average, respectively. The REE concentrations vary from 215 to 420 ppm (~290 ppm on average) and reflect strong LREE-enrichment ($(La/Yb)_N$ values of 12 - 38, and ~20 on average) and anomalously low Eu contents (Eu/Eu^* of ~0.3).

4.2.2 Footslope profile

The soil pH increases gradually from ~4.5 to ~8 from the top to the bottom of the profile (Fig. 8), although the rate of change of pH is more pronounced from the pedolith to the transition zone and is low in the saprock zone. There are, however, abrupt increases in pH at the pedolith-saprolite interface (from 5.2 to 5.8), the saprolite-saprock interface (from 6.5 to 7.0), and the saprock-bedrock interface (from 7.4 to >8) (Fig. 8). The uppermoist soils (top 0.5 m) have the highest TOC content of the entire profile (1.4 wt.%) (Table S2). Below this, the TOC drops to <0.2 wt.% in the pedolith and saprolite zones, and decreases gradually to a minimum of 0.01 wt.% at the saprock-saprolite interface, before increasing to 0.05 wt.% in the first four meters of the saprock zone.

We applied the Chemical Index of Alteration (CIA = [(Al_2O_3 / (Al_2O_3 + CaO (silicate) + Na_2O + K_2O)) × 100], in molar concentration) (Fig. 8) to evaluate the degree of weathering, Values of this index increase gradually from 51 - 53 in the fresh granite to 53 - 61 in the saprock. However, there are sharp increases in the CIA values of the saprock at depths of ~13 and 18 m, corresponding to some densely jointed intervals. The CIA values increase abruptly to 67 in the lower saprolite, and there is another abrupt increase at the saprolite-pedolith interface, from 73 to 78 before a small decrease to 75 in the uppermost soils. Major element concentrations vary with depth in the profile (Fig. 8). The SiO_2 content is relatively constant at 75 - 78 wt.% in the saprock but rises sharply to a maximum of >80 wt.% at the saprock-saprolite interface. In the saprolite, the SiO_2 content decreases gradually to 68 wt.% at the saprolite-pedolith interface, and in the pedolith, it varies from 68 to 76 wt.%. The trends of Al_2O_3 and Fe_2O_3 contents are opposite to that of SiO_2 (Fig. 8). In the saprock, the contents are in the range, 11.3 - 12.3 and 1.26 - 2.76 wt.%, respectively. They drop to minima of 9.31 and 1.32 wt.%, respectively, at the saprock-saprolite interface, and increase slightly in the lower saprolite, reaching maxima of ~17.5 and 3.5 wt. %, respectively, at the saprolite-pedolith interface. The contents of both oxides vary considerably in the pedolith, with Al_2O_3 ranging between 12.8 and 17.5 wt. % and

334 Fe_2O_3 ranging between 1.79 - 3.46 wt. %, respectively. Overall, the values are higher in the
335 lower pedolith and decrease gradually in the upper pedolith towards the surface. The alkali
336 (Na_2O and K_2O) contents are relatively constant in the saprock with values of 6.73 to 8.01
337 wt.%, but there is a local minimum at a depth of ~13 m, corresponding to the sharp increase in
338 the CIA value. An abrupt drop in alkali content is also observed at the saprock-saprolite
339 interface from 6.90 to 5.30 wt. %. In the saprolite and lower pedolith, the alkali content
340 decreases progressively from ~6.5 to 2.9 wt. % but fluctuates with decreasing depth and
341 increases to ~4 wt. % at the top of the profile (Fig. 8).

342 In contrast to the behavior of the major elements, the REE concentration varies greatly
343 (Fig. 9 and 10; Table S2). It increases from ~250 ppm in the bedrock to 360 ppm in the saprock,
344 on average, and this change is gradual for the 2 - 3 m of saprock immediately overlying the
345 bedrock. Above this, the variation in the REE concentration in the saprock is small, except for
346 an abrupt decrease from ~420 to ~300 ppm at a depth of ~13 m (for which significant decreases
347 in SiO_2 and alkali contents have been noted). There is another significant decrease in the REE
348 concentration at a depth of 8.5 m (from ~430 to 260 ppm), which coincides with the occurrence
349 of a well-jointed interval. The REE concentration reaches a maximum of ~670 ppm at the
350 saprock-saprolite interface and decreases sharply above and below this point. In the saprolite,
351 the REE concentration fluctuates between 270 and 410 ppm, the latter of which is observed at
352 a depth of ~3.9 m, and reaches another peak, ~520 ppm, at the saprolite-pedolith interface. The
353 REE concentration continues to fluctuate in the lower pedolith, where it reaches a local
354 maximum of ~460 ppm at a depth of 1.4 m, above which it decreases progressively. Overall,
355 the REE behave similarly, except for Ce, especially at the saprock-saprolite interface at ~6.5
356 m where it is anomalously high, and also at ~3.9 m, where there is a smaller spike in
357 concentration. The $(La/Yb)_N$ ratio varies considerably in the profile but generally increases
358 from the pedolith to the transition zone. In the saprock, the $(La/Yb)_N$ value does not vary

359 significantly but decreases in the highly-jointed interval, where there is an enrichment of the
360 HREEs (Fig. 9). There is an abrupt drop from ~10 to 3 in the uppermost soils above a depth of
361 0.4 m, which also corresponds to an enrichment of the HREEs (Fig. 9 and 10). The parent rock-
362 normalized Ce anomaly reaches a maximum of 16 at this depth and, after initially decreasing,
363 increases to a value of ~6 at the saprolite-pedolith interface. In the saprolite, the Ce anomaly
364 gradually decreases with depth, except at a depth of ~3.9 m, where it peaks locally. Another
365 peak (Ce*/Ce = 13) is observed at the saprock-saprolite interface below which the Ce anomaly
366 gradually increases with depth in the saprock. The results described above are reported in Table
367 S2.
368
369 **4.2.3 Upslope profile**
370 In the upslope profile, the CIA value rises consistently from 82 to 87 in the pedolith but
371 drops abruptly to 80 in the uppermost soils, whereas the soil pH varies slightly from 4.7 to 5.1
372 (Table S2). The TOC content decreases gradually from ~0.10 to 0.04 wt.% down the profile.
373 The SiO_2 content increases from 73 wt.% in the saprolite to 80 wt.% at the saprolite-pedolith
374 interface, but then decreases to ~70 wt.% in the pedolith. Both Al_2O_3 and Fe_2O_3 vary inversely
375 to SiO_2, with average contents decreasing from 14.7 to 10.3 wt.% and from 3.2 to 2.0 wt.%,
376 respectively, from the saprolite to the saprolite-pedolith interface and increasing to 17.3 and
377 3.1 wt. %, respectively, in the pedolith. The average content of alkalis also decreases from the
378 saprolite to the saprolite-pedolith interface (from 3.0 to 1.9 wt.%) and rises to 2.8 wt.% in the
379 pedolith. The total REE content of the saprolite is ~600 ppm and reaches a maximum of ~1,000
380 ppm in the lower pedolith. Above this, it decreases gradually to ~650 ppm. The $(La/Yb)_N$ value
381 gradually increases from 13 at the top of the profile to 20 in the lower pedolith and then
382 decreases to 15 in the saprolite (Fig. 10). In general, the Ce anomaly increases progressively

383 from the bottom to near the top of the profile, with Ce*/Ce reaching a maximum of 2.6 at a
384 depth of 0.55 m.
385
386 **4.2.4 Ridgetop profile**
387 In the ridgetop profile, the CIA value generally increases from 74 in the saprolite to 77
388 at the top of the profile (Table S2). The soil pH increases progressively from 5.6 to 6.2 from
389 the top to the bottom of the profile, whereas the TOC content gradually decreases from 0.08
390 wt.% at the top to 0.02 wt.% at the bottom. In contrast to the upslope profile, SiO_2, and Al_2O_3
391 contents vary in the same way, from 81 to 77, and 10 to 13 wt.%, from the bottom to the top to
392 the profile, respectively. The Fe_2O_3 content slightly decreases from 1.6 wt.% in the saprolite to
393 1.2 wt.% at the saprolite-pedolith interface but then increases up to 2.2 wt.% in the pedolith.
394 There is little variation in the content of the alkalis which ranges from 3.26 to 3.61 wt.%. In
395 this profile, REE concentration reaches an exploitable grade of between 900 and 1,200 ppm.
396 The entire profile is LREE-rich, compared to the parent granite, with $(La/Yb)_N$ values of 25 –
397 33 and the average value is 20 (Fig. 10). All the REEs behave similarly in this profile as does
398 the Ce*/Ce value, which varies between 1.1 and 1.3.
399
400 **4.3 Mass changes during weathering**
401 To evaluate the elemental gain and loss during progressive weathering, mass balance
402 calculations were performed. This involved evaluating the element-mass-transfer coefficient,
403 $\tau_{j,w}$, calculated by the concentration of element j in weight percent, C_j and that of an immobile
404 element i, C_i, as:$\tau_{j,w} \equiv \frac{C_{j,w}C_{i,p}}{C_{j,p}C_{i,w}} - 1$
405
$$\tau_{j,w} \equiv \frac{C_{j,w}C_{i,p}}{C_{j,p}C_{i,w}} - 1$$

406 Subscripts *w* and *p* refer to the weathered material and parent rock, respectively. The average
407 composition of 10 samples of unweathered granite from the drill core were used to represent
408 the elemental concentration in the parent rock and Zr was assumed to be immobile as primary
409 zircon, the host for this element, was not affected by weathering. The results of the calculation
410 are illustrated in Figure 11 - 13.
411
412 **4.3.1 Footslope profile**
413 Based on the above calculation, most of the major elements, including Si, Al, Fe, and
414 K were conserved in the saprock, especially in the lower part. There is, however, a significant
415 loss of Na in the saprock, generally ~30% and locally up to ~50% by mass. In contrast to the
416 major elements, the REE are consistently gained in saprock that is >4 m above the bedrock,
417 generally by 20 to 50%. At the saprock-saprolite interface, there is a mass gain of 350% in Ce,
418 whereas immediately below this interface Ce is lost in proportions reaching 50% by mass. In
419 the same interval, however, the other REE are generally gained in proportions of 60 - 80% by
420 mass. It is also noteworthy that in the interval where Ce is lost, there is a mass gain of 40 - 80%
421 in Fe. In the saprolite and pedolith, both Si and K are lost progressively with decreasing depth,
422 with the mass losses reaching ~40 and 60%, respectively, whereas Na is completely lost in this
423 interval. Iron is generally conserved in the lower saprolite but gained in the upper pedolith zone,
424 although the magnitude of the gain varies; it reaches a maximum (120% by mass) at the
425 saprolite-pedolith interface. Aluminum is largely conserved in the saprolite and pedolith zones,
426 but experiences a 60% mass gain near the saprolite-pedolith interface. Overall, the trends in
427 the REE follow those of the major elements. The REE are generally lost in the lower saprolite
428 (~20% by mass) and upper pedolith zones (~85% by mass) and gained in the upper saprolite
429 and lower pedolith zones (5 - 60% by mass). The HREE display stronger mass gains in this
430 interval, which reach 100% at the saprolite-pedolith interface. Finally, the behavior of Ce is

431 locally decoupled from that of the other REEs (Fig. 11); for example, at a depth of between 4
432 and 6 m, there is significant enrichment of Ce but only moderate enrichment of the other REEs.
433
434 **4.3.2 Upslope profile**
435 In the upslope profile, Si, K, and Na are lost in proportions by mass of 40, 65, and 100%
436 respectively, throughout the profile (Fig. 12). Aluminum is generally conserved, although there
437 is a modest mass gain of 30% in the upper pedolith followed by a mass loss of up to 40% at
438 the top of the profile. Iron is consistently gained in proportions of 40 - 80% by mass but is
439 conserved in the uppermost soils. Except for Ce, the REEs are characterized by significant
440 mass gains throughout the profile. The magnitudes of the mass gains gradually increase from
441 ~100% in the saprolite to a maximum of ~300% in the upper pedolith zone but then decrease
442 abruptly to ~50% in the uppermost part of the profile. The HREEs are preferentially gained.
443 Cerium is generally conserved in the upper and lower parts of the profile but mass gains varying
444 from 20 to 80% are observed in the pedolith.
445
446 **4.3.3 Ridgetop profile**
447 Both Si and Al show evidence of small mass changes in the ridgetop profile, i.e., a gain
448 of <10% at the top of the profile, followed by a loss of <10% in the pedolith and then a gain of
449 ~15% in the upper saprolite (Fig. 13). Iron behaves contrarily, showing significant gains in the
450 pedolith of up to 60% by mass but a loss of 15 - 30% by mass in the saprolite. Potassium and
451 Na are consistently lost by 40 and 100% by mass, respectively. As in the upslope profile, all
452 the REEs except Ce exhibit significant mass gains, varying from 350 to 500%. The mass gain
453 in Ce is relatively constant at ~50% throughout the profile.
454
455 **4.4 The mode of REE occurrence**

To evaluate the behavior of the REE during weathering and, in particular, to distinguish among adsorbed REE, detrital REE and neo-formed REE minerals, we performed sequential extraction experiment on a suite of weathered samples. The adsorbed REE were subdivided into three types, exchangeable REE adsorbed dominantly by clay minerals, Fe-Mn oxyhydroxide-adsorbed REE and organic substance-bound REE. The results of the sequential extraction experiments are shown in Figure 9 and 14 and Table S3.

4.4.1 Footslope profile

The content of the clay-adsorbed portion gradually increases from 60 ppm on average in the uppermost soils to a maximum of ~270 ppm at a depth of 1.4 m and fluctuates with depth in the rest of the pedolith and the saprolite before reaching a peak of ~280 ppm at the saprolite-pedolith interface (~ 6.5 m depth). In contrast to the bulk concentration, which reaches a maximum at the saprock-saprolite interface, the adsorbed REE concentration is exceptionally low, with a concentration of ~120 ppm at this interface. In the saprock, the adsorbed REE concentrations are generally higher and vary less than in the overlying soils, ranging from 170 to 320 ppm. Comparing the adsorbed Ce-excluding REE (abbreviated as REE-Ce in the following text) and Ce concentrations, it is apparent that the adsorbed REE concentrations are largely contributed from the REE-Ce component in the pedolith, saprolite, and transition zones (Fig. 9). In the saprock, the adsorbed Ce concentrations increase progressively with depth, rising from ~15 ppm at the saprock-saprolite interface to 90 ppm at the bottom of the profile.

The proportion of the clay-adsorbed REE rises from ~30% of the total REE in the uppermost soils to ~60% in the pedolith and ~70% in the saprock. As with the bulk REE concentration, the proportion of clay-adsorbed Ce is decoupled from that for the other REEs in the pedolith, saprolite, and transition zones. In the saprock, Ce behaves similarly to the other REEs, and the clay-adsorbed portion of the bulk REE concentration is similarly large (>60%).

The Fe-Mn oxyhydroxide-adsorbed portion is less important and comprises < 20% of the bulk REE concentration, except at the saprolite-pedolith interface and in the transition zone. However, the latter is significant as the Ce concentration peaks at the saprolite-pedolith interface and in the transition zone (Fig. 9). In the transition zone, the Fe-Mn oxyhydroxide-adsorbed portion contributes more than 90% of the bulk Ce concentration. The proportion of organic substance-bound REE is generally very low, although locally it represents up to 10% of the bulk Ce concentration (Fig. 9).

4.4.2 Upslope profile

The clay-adsorbed REE concentration in the upslope profile increases from ~520 ppm (~80% of the total REE content) in the uppermost soils to ~780 ppm (~90%) in the pedolith zone and is relatively unchanged in the rest of the profile, except at the saprolite-pedolith interface, where the concentration drops to ~460 ppm (Fig. 14a). In contrast to the other REE, the clay-adsorbed Ce concentration is roughly constant at ~140 ppm (~70%) throughout the profile. The Fe-Mn oxyhydroxide-bound portion contributes 50 to 100 ppm (<10%) to the total REE concentration and shows no systematic variation with depth in the profile. The organic substance-bound portion is negligible.

4.4.3 Ridgetop profile

In the ridgetop profile, the clay-adsorbed REE concentration varies from 750 (~85% of the total REE concentration) to 950 ppm (~95%) in the pedolith, but decreases to 670 ppm in the saprolite (Fig. 14b). The clay-adsorbed Ce concentration is relatively constant at ~85 ppm (~50% of the total Ce concentration) in the profile. The Fe-Mn oxyhydroxide-bound REE concentration varies between 100 and 150 ppm with Ce generally contributing ~40% of this portion. As in the upslope profile the proportion of organic substance-bound REE is negligible.

506

507 # 5. Discussion

508 ## 5.1 REE dynamics in soil profiles during weathering: a 1-D perspective

509 During weathering, decomposition of the bedrock produces regolith with an upward
510 trajectory from the bottoms of soil profiles, whereas dissolution of minerals at the erosional
511 surface causes downward transport of elements (Anderson et al., 2007). Authigenic minerals,
512 such as clay minerals and Fe oxyhydroxides, form due mainly to physicochemical changes in
513 the profile, such as an increase in pH and Eh. Elemental mobilization and re-distribution in soil
514 profiles is controlled by regolith production, mineral dissolution, supergene mineral
515 precipitation, and adsorption. In the case of the REEs, changes in pH, Eh and other
516 physicochemical parameters may also lead to fractionation of the heavy from the light members
517 of the family. In this section, the footslope profile is used to illustrate the REE dynamics along
518 the soil profile.

519

520 ### 5.1.1 Mobilization and re-distribution of REEs

521 #### 5.1.1.1 Saprock zone

522 In the lower saprock zone, representing the earliest stage of weathering, the REE
523 behaved conservatively (Fig. 11). Weathering of apatite and monazite was negligible, due to
524 the nearly neutral pH, and consequently mobilization of the REE was insignificant. The
525 decomposition of albite and biotite, however, led to removal of major elements and a decrease
526 in the overall mass, creating a small apparent accumulation of the REEs.

527 From the bottom to the top of the saprock zone, representing more advanced weathering,
528 decomposition of primary REE minerals, especially apatite, occurred due to the increase in
529 acidity (Fig. 9). The released REEs were partially retained through precipitation of
530 rhabdophane (Fig. 5c). However, mostly (up to 80%) they were adsorbed on the surface of clay

minerals, mainly kaolinite (Fig. 9; Table S3). In this zone, there was a two- to three-fold enrichment of the REEs (Fig. 9 - 11; Table S2), especially the HREEs, which greatly exceeded the accumulation due to the removal of the major elements (Fig. 11). Hence, it follows that REEs were added to the saprock zone, either from the downward percolating weathering solutions, lateral groundwater flow, or a combination of the two. Although it is impossible to quantitatively estimate the relative contributions of these two end-members, the observation that the saprock zone is below the groundwater table suggests a more important role for the groundwater flow.

5.1.1.2 Saprolite and pedolith zones

In the pedolith layers, representing an advanced stage of weathering, the REE profile is characterized by depletion and enrichment with concentration peaks at a depth of 1.4 m and at the pedolith-saprolite (2.9 m) interface (Fig. 9). The enrichment at these locations is attributed to adsorption on clay minerals, consistent with the high clay-adsorbed proportions (Fig. 9) and can be explained by the abrupt increase in the soil pH at the pedolith-saprolite interface (Fig. 9). This rise in the soil pH would have favored REE adsorption on clay minerals (Coppin et al., 2002), especially kaolinite, for which the cation exchange capacity is dominated by pH-dependent negative charge sites from broken bonds and lattice defects (Ma and Eggleton, 1999; Wilson et al., 2013). The lower soil pH above this interface, due to the input of surficial organic matter and slightly acidic meteoric water into the soil solutions, would have led to leaching of the adsorbed REEs from kaolinite, thereby explaining the lower total REE concentrations. The gradual increase in soil pH downward in the soil profile (Fig. 9), due to continuous mineral-fluid interaction, would have promoted the adsorption of REE on kaolinite. This explains the correspondingly higher proportion of clay-adsorbed REE (Fig. 9). As this part of the soil profile

555 is above the local groundwater table most of the time, vertical infiltration and mineral-fluid
556 interaction would have been the main controls on REE dynamics.

557 As a result of the combined effects of chemical weathering and denudation, element
558 concentration peaks migrate towards the surface with time (Nesbitt and Markovics, 1997). It is
559 therefore possible that the REE concentration peak at 1.4 m may represent a "relict" pedolith-
560 saprolite interface that has migrated upwards into the pedolith horizon and has been
561 deteriorating because of more intense acidic leaching near the surface and the migration of the
562 REE from the shallow soils to the deeper parts of the profile.

563

564 **5.1.2 LREE-HREE fractionation**

565 The role of the primary REE mineralogy, REE complexation, and external REE input
566 on REE fractionation during weathering has been discussed extensively in previous studies
567 (Banfield and Eggleton, 1989; Braun et al., 1993; Johannesson and Lyons, 1994; Harlavan and
568 Erel, 2002; Braun et al., 2018). Here, we examine the relative importance of these factors to
569 the behavior of the REE in the different zones of the regolith in the study area.

570 In the saprock zone, lateral groundwater flow largely controls the REE dynamics.
571 External input of HREE-rich groundwater (Li et al., 2019) enriches the saprock in the HREEs,
572 particularly in the highly jointed part. Thus, the saprock zone generally has a lower $(La/Yb)_N$
573 value than the parent granite (Fig. 9 and 10).

574 Overall, the saprolite and pedolith zones are more enriched in the HREEs compared to
575 the parent granite, especially the upper pedolith zone (Fig. 9, 10 and 14). This suggests that
576 acidic leaching of LREE-bearing minerals efficiently removed the LREEs from the soils,
577 whereas the HREEs were largely retained in refractory zircon and xenotime. In the lower
578 pedolith zone, the increase in the soil pH favors the adsorption on kaolinite (Coppin et al.,
579 2002), preferentially scavenging the LREEs from the soil solutions, as indicated by the high

580 $(La/Yb)_N$ values of the clay-adsorbed portions (Table S3). Stronger complexation of the
581 HREEs with dissolved carbonate ions than of the LREEs with these species also helps explain
582 the retention of the HREEs in the soil solutions (Cantrell and Byrne, 1987; Wood, 1990; Lee
583 and Byrne, 1993; Johannesson and Lyons, 1994; Johannesson et al., 1996). This would have
584 increased the proportion of LREE available for adsorption on kaolinite, consistent with the
585 observation that with depth in the pedolith zone there is a shift in the bulk $(La/Yb)_N$ ratio to
586 higher values (Fig. 9 and 10). In the saprolite zone, a preferential LREE enrichment from the
587 upper towards the lower saprolite zone is also evident (Fig. 9). This is probably because the
588 soil solutions became depleted in the LREEs, due to adsorption on kaolinite, along the
589 infiltration path. Thus, the soil solutions scavenged the LREEs from the regolith in the upper
590 saprolite zone, causing the drop in both the $(La/Yb)_N$ value and clay-adsorbed REE
591 concentration (Fig. 9).
592
593 **5.1.3 Origin of the Ce anomalies**
594 The behavior of Ce is usually different from that of the other REEs during weathering
595 because Ce occurs dominantly as Ce^{4+} and commonly precipitates as cerianite [CeO_2] whereas
596 the other REEs occur in the 3+ state and are leached by the weathering solutions (Braun et al.,
597 1990; Braun et al., 1998; Duzgoren-Aydin and Aydin, 2009; Babechuk et al., 2014; Berger et
598 al., 2014; Janots et al., 2015; Su et al., 2017; Braun et al., 2018). The ratio of Ce^{4+}/Ce^{3+} will
599 vary with the Eh, which, when high, will lead to very high Ce^{4+}/Ce^{3+} ratios and positive Ce
600 anomalies such as that at the depth of ~0.5 m (Fig. 9 and 11; Table S2). In the saprolite zone,
601 decoupling of Ce from the other REEs may be due to seasonal fluctuations of the groundwater
602 table between wet and dry seasons. The groundwater table represents a contrasting redox front
603 and its fluctuation results in development of a series of oxic fronts at different depths (Braun
604 et al., 1990; Ma et al., 2007). The saprock-saprolite interface at 6.5 m, which is characterized

by an unusually strong positive Ce anomaly, represents a long-term oxic front; the smaller positive anomalies higher in the saprolite zone could represent shorter-lived oxic fronts. Coincidentally, the saprock-saprolite interface is marked by a very high proportion of Ce adsorbed by Fe-Mn oxyhydroxides (Fig. 9). The close spatial relationship between Fe-Mn oxyhydroxides and cerianite precipitates suggests that oxidation of Ce^{3+} to Ce^{4+} was very likely catalyzed by these Fe-Mn oxyhydroxide phases (Bau, 1999; Davranche et al., 2005; Davranche et al., 2008).

5.2 REE dynamics in sub-tropical hillslope evolution: a 2-D perspective

5.2.1 Hillslope morphology, erosion and chemical weathering

The intensity of chemical weathering and the rate of denudation may vary considerably in the different parts of a hillslope, and determine the evolution of the weathering crusts (Taylor and Eggleton, 2001; Schaetzl and Anderson, 2005; Schaetzl, 2013). In the studied catchment, the soil profile thickens from the ridgetop downslope (Fig. 1).

Assuming steady state denudation and non-linear transport along hillslope, the relationship between the denudation rate and the hillslope morphology can be quantitatively constrained from the dimensionless relief function, R*, and the dimensionless denudation rate, D*, using the equation:

$$R^* = \frac{R}{S_c L_H} = \frac{1}{D^*}\left[\sqrt{1+(D^*)^2} - In\left(\frac{1}{2}\left(1+\sqrt{1+(D^*)^2}\right)\right) - 1\right] \quad (1)$$

in which S_c is the critical slope gradient, L_H is the hillslope length from the ridgetop to the slope toe, and R is the hillslope relief, defined as the elevation difference between the ridgetop and the slope toe (after Roering et al., 2007). Assuming that S_c is 1.2, based on the similarity of the studied site to the sites considered by Roering et al. (2007), the calculated R* and D* values are 0.47 and 3.0, respectively. This is consistent with the localization of convexity near the ridgetop (Roering et al., 2007).

630 To quantitively describe the mass change for each element in different parts of the
631 hillslope, we used the hillslope evolution model of Jin et al. (2010) and Liu et al. (2016). In
632 this model, our ridgetop and footslope profiles represent the top and bottom ends of the
633 hillslope, respectively, whereas the upslope profile represents the mid-slope. The masses for
634 each profile were calculated by weight-averaging the bulk chemical compositions from the
635 thickness of each sampled interval, except for the footslope profile, for which only the pedolith
636 and saprolite (excluding the transition zone) were considered. The soil production rate per unit
637 area per time was assumed to be equal to the denudation rate per unit area per time, such that:

638 $$P = D = W + E \quad (2)$$

639 in which P, D, W and E are the soil production rate, total denudation rate, chemical weathering
640 rate and erosion rate of the profile. Considering that the absolute denudation rate is not known
641 for our profile, we replaced D in the above equation with D*, the dimensionless denudation
642 rate and were thus only able to determine the relative mass changes as a function of the above
643 parameters. We also assumed that the denudation rate is the same for the different profiles. The
644 dimensionless erosion rate (E*) for the ridgetop profile (Rt) was calculated from the equations:

645 $$D^*C_{i,p} = E^*C_{i,Rt} \quad (3)$$

646 $$D^*C_{j,p} = E^*C_{j,Rt} + W^*_{j,Rt} \quad (4)$$

647 $$E^*_{Rt} = D^*(C_{i,p}/C_{i,Rt}) \quad (5)$$

648 in which C is the concentration of an element and the subscripts
649 i, j and p refer to the immobile element (Zr), the mobile elements and
650 the parent granite. The dimensionless physical erosive output flux (Q*)
651 was calculated from the equation:$Q^*_{Rt} = E^*_{Rt}L$
652 (6)

653 in which L is the length of the box for the output flux. For the hillslope considered here, this
654 length is 18 m, which is 1/3 of the distance between the ridgetop and footslope profiles. The
655 dimensionless chemical weathering rate (W*) is defined as:

656 $$W^*_{Rt} = D^*(1 - C_{i,p}/C_{i,Rt}) \quad (7)$$

657 $$W^*_{j,Rt} = D^*[C_{j,p}-(C_{i,p}/C_{i,Rt})C_{j,Rt}] \quad (8)$$

658 The dimensionless chemical depletion factor (CDF*), describing the contribution of chemical
659 weathering relative to the total denudation flux (Riebe et al., 2003), was calculated from the
660 equations:

661 $$CDF^*_{Rt} = W^*_{Rt}/D^* = 1 - C_{i,p}/C_{i,Rt} \quad (9)$$

662 $$CDF^*_{j,Rt} = 1 - (C_{j,Rt}/C_{i,p})/(C_{j,p}/C_{i,Rt}) \quad (10)$$

663 As the mid-slope (Ms) receives a net physical erosive input from the hillslope above, the above
664 equations were modified as follows:

665 $$E^*_{Ms} = D^*(C_{i,p}/C_{i,Rt}) - E^*_{Rt}(1 - C_{i,Rt}/C_{i,Ms}) \quad (11)$$

666 $$Q^*_{Ms} = [D^*(C_{i,p}/C_{i,Ms}) + E^*_{Rt}(C_{i,Rt}/C_{i,Ms})]L \quad (12)$$

667 $$W^*_{Ms} = D^*(1 - C_{i,p}/C_{i,Ms}) + E^*_{Rt}(1 - C_{i,Rt}/C_{i,Ms}) \quad (13)$$

668 $$W^*_{j,Ms} = D^*C_{j,p}[1 - (C_{j,Ms}C_{i,p})/(C_{j,p}C_{i,Ms})] + E^*_{Rt}C_{j,Ms}[1 - (C_{j,Ms}C_{i,Rt})/(C_{j,Rt}C_{i,Ms})] \quad (14)$$

669 $$CDF^*_{Ms} = 1 - C_{i,p}/C_{i,Ms} + E^*_{Rt}/D^*(1 - C_{i,Rt}/C_{i,Ms}) \quad (15)$$

670 $CDF^*_{j,Ms}$ =

671 $$C_{j,p}[1 - (C_{j,Ms}C_{i,p})/(C_{j,p}C_{i,Ms})] + (E^*_{Rt}C_{j,Ms}/D^*)[1 - (C_{j,Ms}C_{i,Rt})/(C_{j,Rt}C_{i,Ms})] \quad (16)$$

672 These dimensionless parameters show the relative intensity of the corresponding hillslope
673 processes. Application of these equations (Table 1), shows that the erosion rate is highest at
674 the ridgetop (3.05), and decreases considerably at the mid-slope (1.52) but increases again at
675 the footslope (2.96). They also show that, whereas chemical weathering barely contributes to
676 denudation at ridgetop, it is important at the mid-slope and footslope. Consequently, the
677 relative CDF values for the major elements, including Si (-0.04), Ti (-0.31), Al (-0.01), and Fe

(-0.06) are negative, indicating the net accumulation of these elements at the ridgetop. Mobile elements, such as Ca (0.90), K (0.37), and Na (1.00), however, are chemically depleted with positive relative CDF values. At the mid-slope and footslope, there is a net accumulation of Fe (-0.88) and Ti (-0.14), whereas most of the other major elements are chemically depleted. The REEs show consistent net accumulation at the ridgetop (e.g., -3.96 for La; -3.36 for Nd; and -2.43 for Yb) and mid-slope (e.g., -1.20 for La; -1.07 for Nd; and -1.86 for Yb) (Table 1). However, the magnitude of net LREE accumulation decreases much more than does that of the HREEs from the ridgetop to the mid-slope. Moreover, chemical weathering contributes to the loss of the LREEs at the mid-slope, as indicated by the positive W* values, but this is not the case for the HREEs. At the footslope, most REEs, except Ce (CDF* of -1.02) and from Er (CDF* of -0.07) to Lu (CDF* of -0.18), and Y (CDF* of -0.01), are chemically depleted due almost entirely to chemical weathering. Hence, there is a preferential depletion of the LREEs downslope. Not surprisingly, Ce behaves differently from the other REE, showing a small net accumulation throughout the entire hillslope.

To summarize, the ridgetop is subjected to strong erosion, whereas chemical weathering increases in importance downslope. At the ridgetop, intense erosion efficiently exposed the deeply buried regolith and removed considerable amounts of many of the components of the major minerals, such as the feldspars, biotite, and chlorite, together with organic matter. At the mid-slope, where the slope convexity decreases and the surface curvature becomes progressively more planar, the downslope-transport of silicate minerals and organic matter enhances the chemical weathering rate (Liu et al., 2016), resulting in larger relative CDF values for most of the major elements.

5.2.2 The Differential behavior of the REE

Intense chemical weathering is commonly coupled with a high denudation rate, as intense erosion will expose the unweathered bedrock rapidly (Anderson et al., 2002; Riebe et al., 2004), leading to efficient release of the REE from the bedrock to the regolith. The soil residence time will be therefore much shorter at the ridgetop than at the footslope, which leads to a more immature soil at the ridgetop with a comparatively low TOC content (Table S2), higher soil pH (Table S2), and a strongly negative Ce anomaly (Fig. 16). As negative Ce anomalies usually develop in the deeper parts of the profiles (Braun et al., 1990; Braun et al., 1998; Sanematsu et al., 2013; Li et al., 2019), a strongly negative Ce anomaly reflects a prolonged burial history and recent exposure of the surficial regolith. Whereas the intense denudation quantitatively removed the major elements (Fig. 12 and 13), the REEs were largely retained, especially for the LREEs (Fig. 10; Table 1). It is likely that adsorption on clay minerals (>75% of the bulk concentration) was responsible for efficiently accumulating the REEs to exploitable grades in the profile (Fig. 12; Table S2). This reflects the stronger adsorption of the REEs relative to the major alkali and alkali earth elements (Coppin et al., 2002). Moreover, neoformation of abundant kaolinite (Fig. 7; Table S1), due to rapid decomposition of feldspars and biotite in the exposed regolith, facilitates the REE adsorption. In upslope areas, erosion prevails over weathering, and its intensity decreases downslope. Longer soil residence times enable vertical REE mobilization and the development of REE depletion-enrichment profiles. Oxidation of Ce^{3+} and precipitation of cerianite, partly immobilized Ce in the shallow soils, thereby decreasing the magnitude of negative Ce anomalies in the regolith compared to the ridgetop profile, whereas the other REE were mobilized downslope (Fig. 16). At the footslope, the denudation rates are likely much lower and regolith formation dominant.

Downslope REE transport modifies the REE distribution in the catchment. Material transport via subsurface throughflow and groundwater flow are probably dominant,

727 considering the high precipitation and infiltration of the sub-tropical regime and absence of
728 evidence of recent or old landslides. As discussed above, groundwater could play a major role
729 in transporting the REEs, especially the HREEs, from the ridgetop to the footslope. Hence,
730 regolith at the ridgetop is less enriched in the HREEs compared to those at the mid-slope and
731 the footslope (Fig. 10). Further evidence for this is provided by the similarity of the enrichment
732 of the REE profiles for the saprock zone to those for the footslope and upslope profiles (Fig.
733 15 and 16), and a net accumulation of the HREEs downslope (Table 1). Input of the REE from
734 groundwater flow also enriched the highly-jointed interval of the saprock zone with the HREEs
735 (Fig. 11 and 16).
736
737 **5.3 Implications for ore formation**
738 Regolith-hosted REE deposits are the products of weathering, in which the REEs
739 accumulated to economically exploitable grades. The case study presented here nicely
740 illustrates the dynamics of REE mobilization during sub-tropical weathering of granitic
741 catchments and the interplay of geomorphological and hydrogeological processes in
742 controlling the spatial distribution of enriched and economically exploitable soils (>0.08 wt. %
743 RE oxide) in the upslope areas and depleted (<0.08 wt. % RE oxide) soils in the footslope.
744 Lateral material flow along catena during hillslope evolution also affects the REE
745 distribution. Although downslope material fluxes transport the REEs to the footslope, REE
746 influx affects the downslope catena evenly due to the moderating influence of the groundwater,
747 resulting in broader and more consistent enrichment zones in the footslope (Fig. 9). On the
748 other hand, REE enrichment in the upslope areas is greatly influenced by the interplay between
749 denudation and chemical weathering. In this case study, a narrow but high-grade REE
750 enrichment zone was identified in the upslope area (Fig. 16). The rate of chemical weathering
751 is high, as is the rate of denudation, and thus, there was efficient liberation of the REEs from

752 the parent rock. However, thick weathering crusts can develop during periods when the
753 denudation rate is low (Schaetzl, 2013). During these periods, the REEs will circulate and re-
754 distribute in the soil profiles. Hence, repeated periods of high and low denudation rates would
755 ensure continued supply of REE from the parent rocks and, through re-mobilization of the REE
756 in thick weathering crusts, combine to create the giant regolith-hosted REE deposits.
757

758 **6. Conclusions**

759 Mobilization of the REE from their parental granites and their distribution within
760 weathering crusts varies with the climate and the geomorphological setting. During sub-
761 tropical weathering, the primary REE mineralogy exerts a major control on the behavior of the
762 REE initially. In this case study, apatite and monazite-(Ce), are the major primary REE
763 minerals, and were relatively unaffected during the incipient stage of weathering. Consequently,
764 REE enrichment at this stage was due mainly to the loss of mass that accompanied the
765 breakdown of the major rock-forming minerals. Oxidation and pH change are the factors
766 controlling the behavior of the REE during advanced weathering, with pH controlling he
767 adsorption of REE, especially the LREE on clay minerals; the latter is evident from the
768 coincidence of peaks in the soil profile for pH and the proportion of clay-adsorbed REE. Oxic
769 fronts, likely derived from seasonal fluctuations in the groundwater table, catalyze the
770 precipitation of Ce as cerianite and/ or Ce scavenging by neo-formed Fe and Mn oxyhydroxides,
771 resulting in Ce accumulation and strongly positive Ce anomalies. On hillslopes that are
772 typically convex-concave in sub-tropical environments, the dominance of denudation in the
773 upslope areas ensures continued exposure of fresh parental material for chemical weathering,
774 thereby releasing more REEs to the regolith, causing considerable enrichment at the ridgetop.
775 Intense erosion could also significantly remove the major minerals at the ridgetop, apparently
776 accumulating the REEs, which are largely retained though adsorption on kaolinite. Towards

777 the footslope, groundwater plays a vital role in the downslope elemental flux, enriching the
778 lower part of the footslope profile in the HREEs.
779
780 **Acknowledgements**
781 We would like to thank the assistance of Drs. Wen Winston Zhao and Zeriu Liu for assistance
782 in the field, Ms. Xiao Fu for XRF analysis, Profs. Liang Qi and Jianfeng Gao from IGCAS,
783 Prof. Xiang-Dong Li and Ms. Carmen Ip from PolyU for trace elemental analysis, and Mr.
784 Jiacheng Liu for aid with the XRD analyses. This study was supported financially by grants
785 from the National Natural Science Foundation of China (91962216 and 41772087) and by
786 China University of Geosciences (Wuhan) to M.-F.Z. and a visiting professorship of HKU to
787 A.W.-J.
788
789 **References**
790 Anderson, S. P., Dietrich, W. E., and Brimhall Jr, G. H., 2002, Weathering profiles, mass-
791 balance analysis, and rates of solute loss: Linkages between weathering and erosion in
792 a small, steep catchment: Geological Society of America Bulletin, v. 114, p. 1143-
793 1158.
794 Anderson, S. P., von Blanckenburg, F., and White, A. F., 2007, Physical and chemical
795 controls on the critical zone: Elements, v. 3, p. 315-319.
796 Aubert, D., Stille, P., and Probst, A., 2001, REE fractionation during granite weathering and
797 removal by waters and suspended loads: Sr and Nd isotopic evidence: Geochimica et
798 Cosmochimica Acta, v. 65, p. 387-406.
799 Babechuk, M., Widdowson, M., and Kamber, B., 2014, Quantifying chemical weathering
800 intensity and trace element release from two contrasting basalt profiles, Deccan Traps,
801 India: Chemical Geology, v. 363, p. 56-75.

802 Banfield, J. F., and Eggleton, R. A., 1989, Apatite replacement and rare earth mobilization,
803 fractionation, and fixation during weathering: Clays and Clay Minerals, v. 37, p. 113-
804 127.
805 Bao, Z., and Zhao, Z., 2008, Geochemistry of mineralization with exchangeable REY in the
806 weathering crusts of granitic rocks in South China: Ore Geology Reviews, v. 33, p.
807 519-535.
808 Bau, M., 1999, Scavenging of dissolved yttrium and rare earths by precipitating iron
809 oxyhydroxide: experimental evidence for Ce oxidation, Y-Ho fractionation, and
810 lanthanide tetrad effect: Geochimica et Cosmochimica Acta, v. 63, p. 67-77.
811 Berger, A., Janots, E., Gnos, E., Frei, R., and Bernier, F., 2014, Rare earth element
812 mineralogy and geochemistry in a laterite profile from Madagascar: Applied
813 geochemistry, v. 41, p. 218-228.
814 Braun, J.-J., Marechal, J.-C., Riotte, J., Boeglin, J.-L., Bedimo, J.-P. B., Ngoupayou, J. R. N.,
815 Nyeck, B., Robain, H., Sekhar, M., and Audry, S., 2012, Elemental weathering fluxes
816 and saprolite production rate in a Central African lateritic terrain (Nsimi, South
817 Cameroon): Geochimica et Cosmochimica Acta, v. 99, p. 243-270.
818 Braun, J.-J., Pagel, M., Herbilln, A., and Rosin, C., 1993, Mobilization and redistribution of
819 REEs and thorium in a syenitic lateritic profile: a mass balance study: Geochimica et
820 Cosmochimica Acta, v. 57, p. 4419-4434.
821 Braun, J.-J., Pagel, M., Muller, J.-P., Bilong, P., Michard, A., and Guillet, B., 1990, Cerium
822 anomalies in lateritic profiles: Geochimica et Cosmochimica Acta, v. 54, p. 781-795.
823 Braun, J.-J., Viers, J., Dupré, B., Polve, M., Ndam, J., and Muller, J.-P., 1998, Solid/liquid
824 REE fractionation in the lateritic system of Goyoum, East Cameroon: the implication
825 for the present dynamics of the soil covers of the humid tropical regions: Geochimica
826 et Cosmochimica Acta, v. 62, p. 273-299.

827 Braun, J. J., Riotte, J., Battacharya, S., Violette, A., Oliva, P., Prunier, J., Maréchal, J. C.,
828 Ruiz, L., Audry, S., and Subramanian, S., 2018, REY-Th-U Dynamics in the Critical
829 Zone: Combined Influence of Reactive Bedrock Accessory Minerals, Authigenic
830 Phases, and Hydrological Sorting (Mule Hole Watershed, South India):
831 Geochemistry, Geophysics, Geosystems, v. 19, p. 1611-1635.
832 Brimhall, G. H., Ford, C., Bratt, J., Taylor, G., and Warin, O., 1991, Quantitative
833 geochemical approach to pedogenesis: importance of parent material reduction,
834 volumetric expansion, and eolian influx in lateritization: Geoderma, v. 51, p. 51-91.
835 Cantrell, K. J., and Byrne, R. H., 1987, Rare earth element complexation by carbonate and
836 oxalate ions: Geochimica et Cosmochimica Acta, v. 51, p. 597-605.
837 Condie, K. C., Dengate, J., and Cullers, R. L., 1995, Behavior of rare earth elements in a
838 paleoweathering profile on granodiorite in the Front Range, Colorado, USA:
839 Geochimica et Cosmochimica Acta, v. 59, p. 279-294.
840 Coppin, F., Berger, G., Bauer, A., Castet, S., and Loubet, M., 2002, Sorption of lanthanides
841 on smectite and kaolinite: Chemical Geology, v. 182, p. 57-68.
842 da Silva, Y. J. A. B., do Nascimento, C. W. A., Biondi, C. M., van Straaten, P., de Souza
843 Júnior, V. S., da Silva, Y. J. A. B., dos Santos, C. A., and de Araújo, J. d. C. T., 2017,
844 Influence of metaluminous granite mineralogy on the rare earth element geochemistry
845 of rocks and soils along a climosequence in Brazil: Geoderma, v. 306, p. 28-39.
846 Davranche, M., Pourret, O., Gruau, G., Dia, A., Jin, D., and Gaertner, D., 2008, Competitive
847 binding of REE to humic acid and manganese oxide: impact of reaction kinetics on
848 development of cerium anomaly and REE adsorption: Chemical Geology, v. 247, p.
849 154-170.
850 Davranche, M., Pourret, O., Gruau, G., Dia, A., and Le Coz-Bouhnik, M., 2005, Adsorption
851 of REE (III)-humate complexes onto MnO 2: experimental evidence for cerium

852 anomaly and lanthanide tetrad effect suppression: Geochimica et Cosmochimica Acta,
853 v. 69, p. 4825-4835.
854 Du, X., Rate, A. W., and Gee, M. M., 2012, Redistribution and mobilization of titanium,
855 zirconium and thorium in an intensely weathered lateritic profile in Western
856 Australia: Chemical Geology, v. 330, p. 101-115.
857 Duddy, L. R., 1980, Redistribution and fractionation of rare-earth and other elements in a
858 weathering profile: Chemical Geology, v. 30, p. 363-381.
859 Duzgoren-Aydin, N., and Aydin, A., 2009, Distribution of rare earth elements and
860 oxyhydroxide phases within a weathered felsic igneous profile in Hong Kong: Journal
861 of Asian Earth Sciences, v. 34, p. 1-9.
862 Elderfield, H., Upstill-Goddard, R., and Sholkovitz, E., 1990, The rare earth elements in
863 rivers, estuaries, and coastal seas and their significance to the composition of ocean
864 waters: Geochimica et Cosmochimica Acta, v. 54, p. 971-991.
865 Foley, N. K., Bern, C. R., Ayuso, R. A., Hubbard, B. E., and Shah, A. K., 2015,
866 Geochemical and mineralogical characteristics of REE in granite-derived regolith: a
867 model for the southeast United States: 13th Biennial Society for Geology Applied to
868 Ore Deposits, 2015.
869 Galán, E., Fernández-Caliani, J., Miras, A., Aparicio, P., and Márquez, M., 2007, Residence
870 and fractionation of rare earth elements during kaolinization of alkaline peraluminous
871 granites in NW Spain: Clay Minerals, v. 42, p. 341-352.
872 García, M. V. R., Krzemień, A., del Campo, M. Á. M., Álvarez, M. M., and Gent, M. R.,
873 2017, Rare earth elements mining investment: It is not all about China: Resources
874 Policy, v. 53, p. 66-76.

875 Goodenough, K. M., Wall, F., and Merriman, D., 2018, The rare earth elements: demand,
876 global resources, and challenges for resourcing future generations: Natural Resources
877 Research, v. 27, p. 201-216.
878 Gouveia, M., Prudencio, M., Figueiredo, M., Pereira, L., Waerenborgh, J., Morgado, I., Pena,
879 T., and Lopes, A., 1993, Behavior of REE and other trace and major elements during
880 weathering of granitic rocks, Evora, Portugal: Chemical Geology, v. 107, p. 293-296.
881 Harlavan, Y., and Erel, Y., 2002, The release of Pb and REE from granitoids by the
882 dissolution of accessory phases: Geochimica et Cosmochimica Acta, v. 66, p. 837-
883 848.
884 Henderson, P., 2013, Rare earth element geochemistry, Elsevier.
885 Huang, J., Sun, S., and Zhang, J., 2013, Detection of trends in precipitation during 1960–
886 2008 in Jiangxi province, southeast China: Theoretical and applied climatology, v.
887 114, p. 237-251.
888 Janots, E., Bernier, F., Brunet, F., Muñoz, M., Trcera, N., Berger, A., and Lanson, M., 2015,
889 Ce (III) and Ce (IV)(re) distribution and fractionation in a laterite profile from
890 Madagascar: Insights from in situ XANES spectroscopy at the Ce L III-edge:
891 Geochimica et Cosmochimica Acta, v. 153, p. 134-148.
892 Jin, L., Ma, L., Dere, A., White, T., Mathur, R., and Brantley, S. L., 2017, REE mobility and
893 fractionation during shale weathering along a climate gradient: Chemical Geology, v.
894 466, p. 352-379.
895 Jin, L., Ravella, R., Ketchum, B., Bierman, P. R., Heaney, P., White, T., and Brantley, S. L.,
896 2010, Mineral weathering and elemental transport during hillslope evolution at the
897 Susquehanna/Shale Hills Critical Zone Observatory: Geochimica et Cosmochimica
898 Acta, v. 74, p. 3669-3691.

899 Johannesson, K. H., and Lyons, W. B., 1994, The rare earth element geochemistry of Mono
900 Lake water and the importance of carbonate complexing: Limnology and
901 Oceanography, v. 39, p. 1141-1154.
902 Johannesson, K. H., Stetzenbach, K. J., Hodge, V. F., and Lyons, W. B., 1996, Rare earth
903 element complexation behavior in circumneutral pH groundwaters: assessing the role
904 of carbonate and phosphate ions: Earth and Planetary Science Letters, v. 139, p. 305-
905 319.
906 Koeppenkastrop, D., and De Carlo, E. H., 1992, Sorption of rare-earth elements from
907 seawater onto synthetic mineral particles: An experimental approach: Chemical
908 geology, v. 95, p. 251-263.
909 Lara, M. C., Buss, H. L., and Pett-Ridge, J. C., 2018, The effects of lithology on trace
910 element and REE behavior during tropical weathering: Chemical Geology, v. 500, p.
911 88-102.
912 Laveuf, C., and Cornu, S., 2009, A review on the potentiality of rare earth elements to trace
913 pedogenetic processes: Geoderma, v. 154, p. 1-12.
914 Lee, J. H., and Byrne, R. H., 1993, Complexation of trivalent rare earth elements (Ce, Eu,
915 Gd, Tb, Yb) by carbonate ions: Geochimica et Cosmochimica Acta, v. 57, p. 295-302.
916 Li, M. Y. H., Zhou, M.-F., and Williams-Jones, A. E., 2019, The genesis of regolith-hosted
917 HREE deposits: Insights from the world-class Zudong deposit in Jiangxi Province,
918 South China: Economic Geology, v. 114, p. 541-568.
919 Li, Y. H. M., Zhao, W. W., and Zhou, M.-F., 2017, Nature of parent rocks, mineralization
920 styles and ore genesis of regolith-hosted REE deposits in South China: An integrated
921 genetic model: Journal of Asian Earth Sciences, v. 148, p. 65-95.

922 Liu, F., and Wu, L., 2017, Study on the characteristics of plant community in the unmined
923 area of rare earth mine in Longnan: China Mining Magazine, v. 26, p. 138-140 (in
924 Chinese with English abstract).
925 Liu, W., Liu, C., Brantley, S. L., Xu, Z., Zhao, T., Liu, T., Yu, C., Xue, D., Zhao, Z., and
926 Cui, L., 2016, Deep weathering along a granite ridgeline in a subtropical climate:
927 Chemical Geology, v. 427, p. 17-34.
928 Ma, C., and Eggleton, R. A., 1999, Cation exchange capacity of kaolinite: Clays and Clay
929 minerals, v. 47, p. 174-180.
930 Ma, J.-L., Wei, G.-J., Xu, Y.-G., Long, W.-G., and Sun, W.-D., 2007, Mobilization and re-
931 distribution of major and trace elements during extreme weathering of basalt in
932 Hainan Island, South China: Geochimica et Cosmochimica Acta, v. 71, p. 3223-3237.
933 Middelburg, J. J., van der Weijden, C. H., and Woittiez, J. R., 1988, Chemical processes
934 affecting the mobility of major, minor and trace elements during weathering of
935 granitic rocks: Chemical Geology, v. 68, p. 253-273.
936 Migoń, P., 2009, Are any granite landscapes distinctive of the humid tropics? Reconsidering
937 multiconvex topographies: Singapore Journal of Tropical Geography, v. 30, p. 328-
938 343.
939 Migoń, P., 2013, Weathering mantles and long-term landform evolution, *in* Shroder, J., and
940 Pope, G. A., eds., Treatise on Geomorphology, 4: San Diego, CA, Academic Press, p.
941 127-144.
942 Mongelli, G., 1993, REE and other trace elements in a granitic weathering profile from
943 “Serre”, southern Italy: Chemical Geology, v. 103, p. 17-25.
944 Murakami, H., and Ishihara, S., 2008, REE mineralization of weathered crust and clay
945 sediment on granitic rocks in the Sanyo Belt, SW Japan and the Southern Jiangxi
946 Province, China: Resource Geology, v. 58, p. 373-401.

947 Nesbitt, H. W., 1979, Mobility and fractionation of rare earth elements during weathering of
948 a granodiorite: Nature, v. 279, p. 206-210.
949 Nesbitt, H. W., and Markovics, G., 1997, Weathering of granodioritic crust, long-term
950 storage of elements in weathering profiles, and petrogenesis of siliciclastic sediments:
951 Geochimica et Cosmochimica Acta, v. 61, p. 1653-1670.
952 Pourret, O., Davranche, M., Gruau, G., and Dia, A., 2007, Organic complexation of rare
953 earth elements in natural waters: evaluating model calculations from ultrafiltration
954 data: Geochimica et Cosmochimica Acta, v. 71, p. 2718-2735.
955 Qi, L., Hu, J., and Gregoire, D. C., 2000, Determination of trace elements in granites by
956 inductively coupled plasma mass spectrometry: Talanta, v. 51, p. 507-513.
957 Riebe, C. S., Kirchner, J. W., and Finkel, R. C., 2003, Long-term rates of chemical
958 weathering and physical erosion from cosmogenic nuclides and geochemical mass
959 balance: Geochimica et Cosmochimica Acta, v. 67, p. 4411-4427.
960 Riebe, C. S., Kirchner, J. W., and Finkel, R. C., 2004, Erosional and climatic effects on long-
961 term chemical weathering rates in granitic landscapes spanning diverse climate
962 regimes: Earth and Planetary Science Letters, v. 224, p. 547-562.
963 Roering, J. J., Perron, J. T., and Kirchner, J. W., 2007, Functional relationships between
964 denudation and hillslope form and relief: Earth and Planetary Science Letters, v. 264,
965 p. 245-258.
966 Roskill, 2011, Rare Earths & Yttrium: Market Outlook to 2015: London, p. 492.
967 Sanematsu, K., Ejima, T., Kon, Y., Manaka, T., Zaw, K., Morita, S., and Seo, Y., 2016,
968 Fractionation of rare-earth elements during magmatic differentiation and weathering
969 of calc-alkaline granites in southern Myanmar: Mineralogical Magazine, v. 80, p. 77-
970 102.

971 Sanematsu, K., Kon, Y., Imai, A., Watanabe, K., and Watanabe, Y., 2013, Geochemical and
972 mineralogical characteristics of ion-adsorption type REE mineralization in Phuket,
973 Thailand: Mineralium Deposita, v. 48, p. 437-451.
974 Sanematsu, K., and Watanabe, Y., 2016, Characteristics and genesis of ion-adsorption type
975 deposits: Reviews in Economic Geology, v. 18, p. 55-79.
976 Schaetzl, R., 2013, Catenas and Soils, *in* Shroder, J., and Pope, G. A., eds.,
977 TreatiseonGeomorphology, 4: SanDiego, CA, AcademicPress, p. 145-158.
978 Schaetzl, R. J., and Anderson, S., 2005, Soils: Genesis and Geomorphology, Cambridge
979 University Press, Cambridge, 832 p.
980 Su, N., Yang, S., Guo, Y., Yue, W., Wang, X., Yin, P., and Huang, X., 2017, Revisit of rare
981 earth element fractionation during chemical weathering and river sediment transport:
982 Geochemistry, Geophysics, Geosystems, v. 18, p. 935-955.
983 Taylor, G., and Eggleton, R. A., 2001, Regolith geology and geomorphology, John Wiley &
984 Sons.
985 Thomas, M., 1994, Geomorphology in the Tropics: A Study of Weathering and Denuation in
986 Low Latitudes, Wiley, 482 p.
987 Wilson, M., Deer, W., Howie, R., and Zussman, J., 2013, Rock-Forming Minerals, Volume
988 3C, Sheet Silicates: Clay Minerals: Geological Society, London, 2013, p. 724.
989 Wood, S. A., 1990, The aqueous geochemistry of the rare-earth elements and yttrium: 1.
990 Review of available low-temperature data for inorganic complexes and the inorganic
991 REE speciation of natural waters: Chemical Geology, v. 82, p. 159-186.
992 Wu, C., Huang, D., and Guo, Z., 1990, REE geochemistry in the weathered crust of granites,
993 Longnan area, Jiangxi Province: Acta Geologica Sinica (English Edition), v. 3, p.
994 193-209.

995 Yusoff, Z. M., Ngwenya, B. T., and Parsons, I., 2013, Mobility and fractionation of REEs
996 during deep weathering of geochemically contrasting granites in a tropical setting,
997 Malaysia: Chemical Geology, v. 349, p. 71-86.
998 Zhang, L., 1989, Some special geomorphic processes of the monsoon area in East China:
999 Catena, v. 16, p. 121-134.

1000

1001 **Figure captions**

1002 **Figure 1**. (a) Location and simplified geological map of the Bankeng deposit (after Li et al.,
1003 2019); (b) satellite image and simplified contour of the study area; and (c) a representative
1004 longitudinal section of the study area. The locations of the soil profiles discussed in the text are
1005 marked on the satellite image and the section. The satellite image was obtained from Google
1006 Earth.

1007

1008 **Figure 2**. A schematic column of the footslope profile with representative photos and
1009 descriptions of the different soil horizons.

1010

1011 **Figure 3**. Petrography and mineralogy of the parent granite. (a) Photomicrograph in cross-
1012 polariszed light showing a myrmekitic intergrowth of quartz and K-feldspar. (b) - (f)
1013 Backscattered electron (BSE) images. (b) Replacement of apatite by monazite-(Ce). (c) An
1014 irregularly-shaped grain of monazite-(Ce). (d) An irregularly-shaped monazite-(Ce) crystal in
1015 contact with a euhedral zircon crystal. (e) A filamentous mass of bastnäsite and an anhedral
1016 monazite-(Ce) crystal. (f) A metasomatized crystal of fergusonite with the darker BSE domain
1017 having lower REE concentration. Abbreviations: Ap: Apatite, Bst: Bastnäsite, Bt: Biotite, Chl:
1018 Chlorite, Fgt: Fergusonite, Kfs: K-feldspar, Mnz: Monazite-(Ce), Qtz: Quartz, Zrn: Zircon.

1019

1020 **Figure 4**. Clay minerals in the regolith. (a) and (c) are BSE images whereas the others are SE
1021 images. (a) Replacement of albite by kaolinite. (b) Association of microcrystalline kaolinite
1022 and halloysite. (c) Pseudomorph of vermiculite (giving darker BSE contrast) from partial
1023 replacement of biotite (giving bright BSE contrast) and subsequent decomposition to form
1024 kaolinite. (d) Occurrence of smectite aggregates on surface of biotite grains. (e) Euhedral
1025 vermicular kaolinite “booklet”. (f) Association of long-tubed halloysite and kaolinite. (a) – (d)

1026 are from the saprolite zone and (e) – (f) are from the pedolith zone. Abbreviations: Ab: Albite,
1027 Ant: Anatase, Bt: Biotite, Hal: Halloysite, Kln: Kaolinite, Sme: Smectite, Vrm: Vermiculite.
1028
1029 **Figure 5**. BSE images of REE-bearing minerals in the regolith. (a) A corroded grain of
1030 monazite-(Ce). (b) A partially decomposed grain of thorite. (c) A corroded grain of monazite-
1031 (Ce) crosscut by a goethite veinlet. (d) A rounded grain of zircon. (e) Rhabdophane and goethite
1032 after biotite and xenotime-(Y). (f) Donut-shaped cerianite. Abbreviations: Bt: Biotite, Cer:
1033 Cerianite, Gt: Goethite, Kln: Kaolinite, Mnz: Monazite-(Ce), Qtz: Quartz; Rhd: Rhabdophane,
1034 Tht: Thorite, Xnm: Xenotime-(Y), Zrn: Zircon.
1035
1036 **Figure 6**. Variations in mineral content with depth in the footslope profile. The stars indicate
1037 the average content of the parent granite.
1038
1039 **Figure 7**. Variations in mineral content with depth in the (a) upslope and (b) ridgetop profiles.
1040
1041 **Figure 8**. Variations in soil pH, CIA, and major elemental concentrations in the footslope
1042 profile.
1043
1044 **Figure 9**. Variations in REE concentration, Ce*/Ce, $(La/Yb)_N$, and the proportions of clay-
1045 adsorbed, Fe-Mn oxyhydroxide-adsorbed, and organic matter-bound REE, REE-Ce, and Ce
1046 concentrations with depth in the footslope profile.
1047
1048 **Figure 10**. Average chondrite-normalized REE pattern for different soil profiles and the
1049 unaltered bedrock.
1050

Figure 11. Variations in the ratios of major element oxides and the REEs (represented by La, Ce, and Yb) with Zr relative to those for unaltered granite with depth in the footslope profile.

Figure 12. Variations in the ratios of major element oxides and the REEs (represented by La, Ce, and Yb) with Zr relative to those for unaltered granite with depth in the upslope profile.

Figure 13. Variations in the ratios of major element oxides and the REEs (represented by La, Ce, and Yb) with Zr relative to those for unaltered granite with depth in the ridgetop profile.

Figure 14. Variations in the proportions of clay-adsorbed, Fe-Mn oxyhydroxide-adsorbed, and organic matter-bound REE, REE-Ce, and Ce concentrations with depth in (a) the upslope profile and (b) the ridgetop profile.

Figure 15. Parent rock-normalized REE profile for different soil horizons of the footslope profile.

Figure 16. A schematic model of REE mobilization and re-distribution along a catena in a sub-tropically weathered granitic catchment. The high-grade zone is indicated in orange.

Li, M.Y.H., Zhou, M.-F., Williams-Jones, A.E., 2020. Controls on the Dynamics of Rare Earth Elements
During Subtropical Hillslope Processes and Formation of Regolith-Hosted Deposits. Economic Geology, 115(5): 1097-1118.

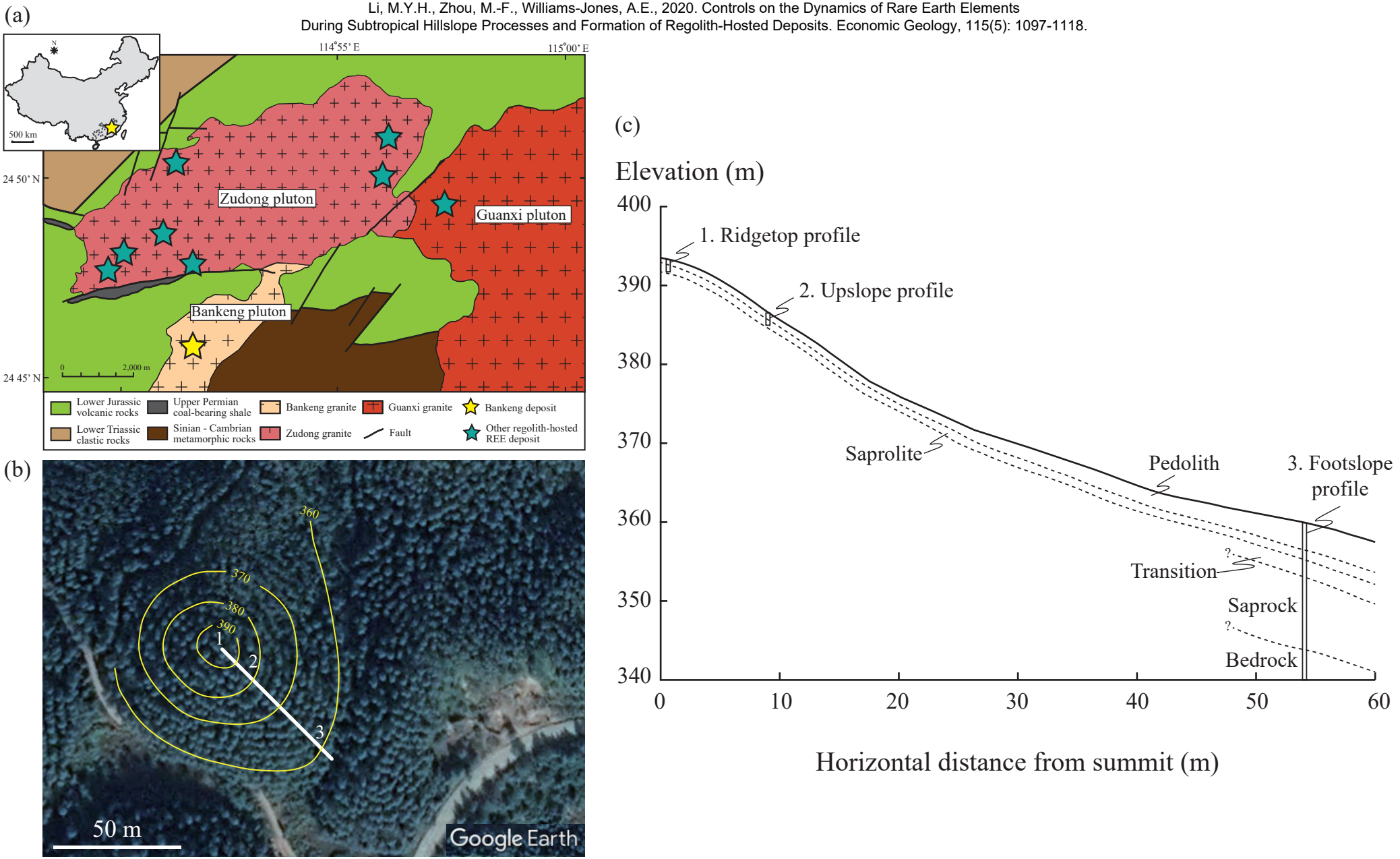

Figure 1

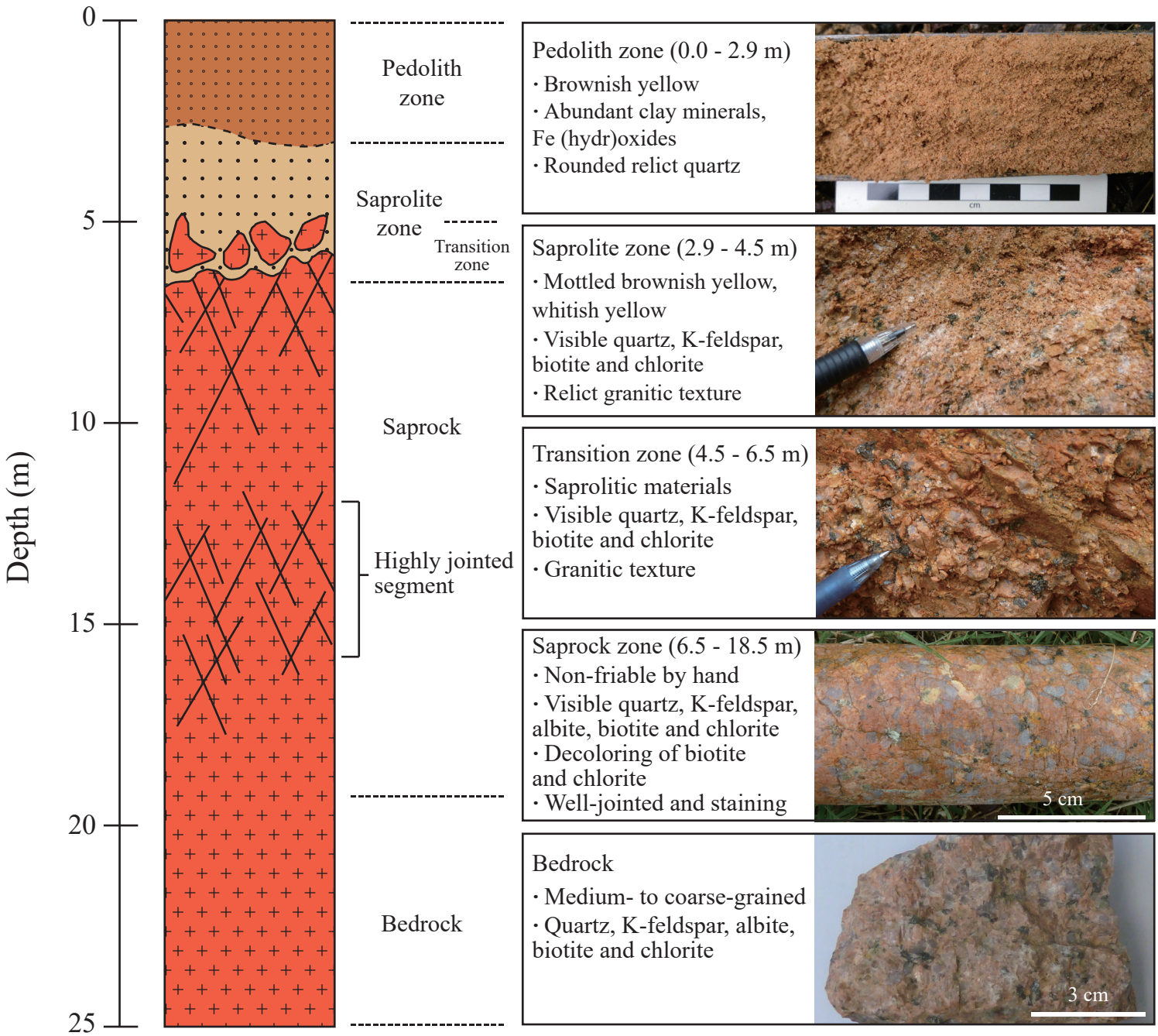

Figure 2

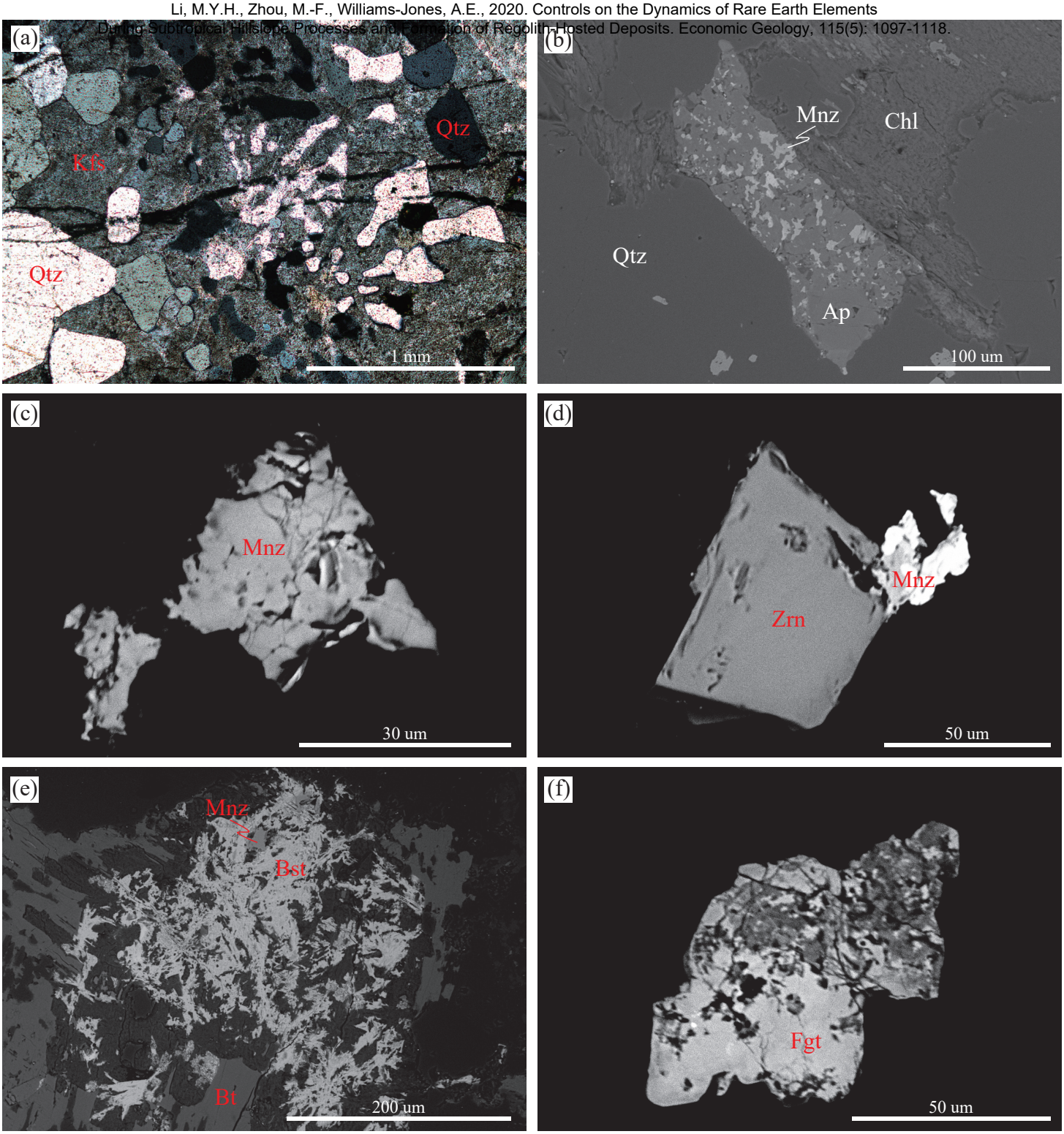

Figure 3

Li, M.Y.H., Zhou, M.-F., Williams-Jones, A.E., 2020. Controls on the Dynamics of Rare Earth Elements
During Subtropical Hillslope Processes and Formation of Regolith-Hosted Deposits. Economic Geology, 115(5): 1097-1118.

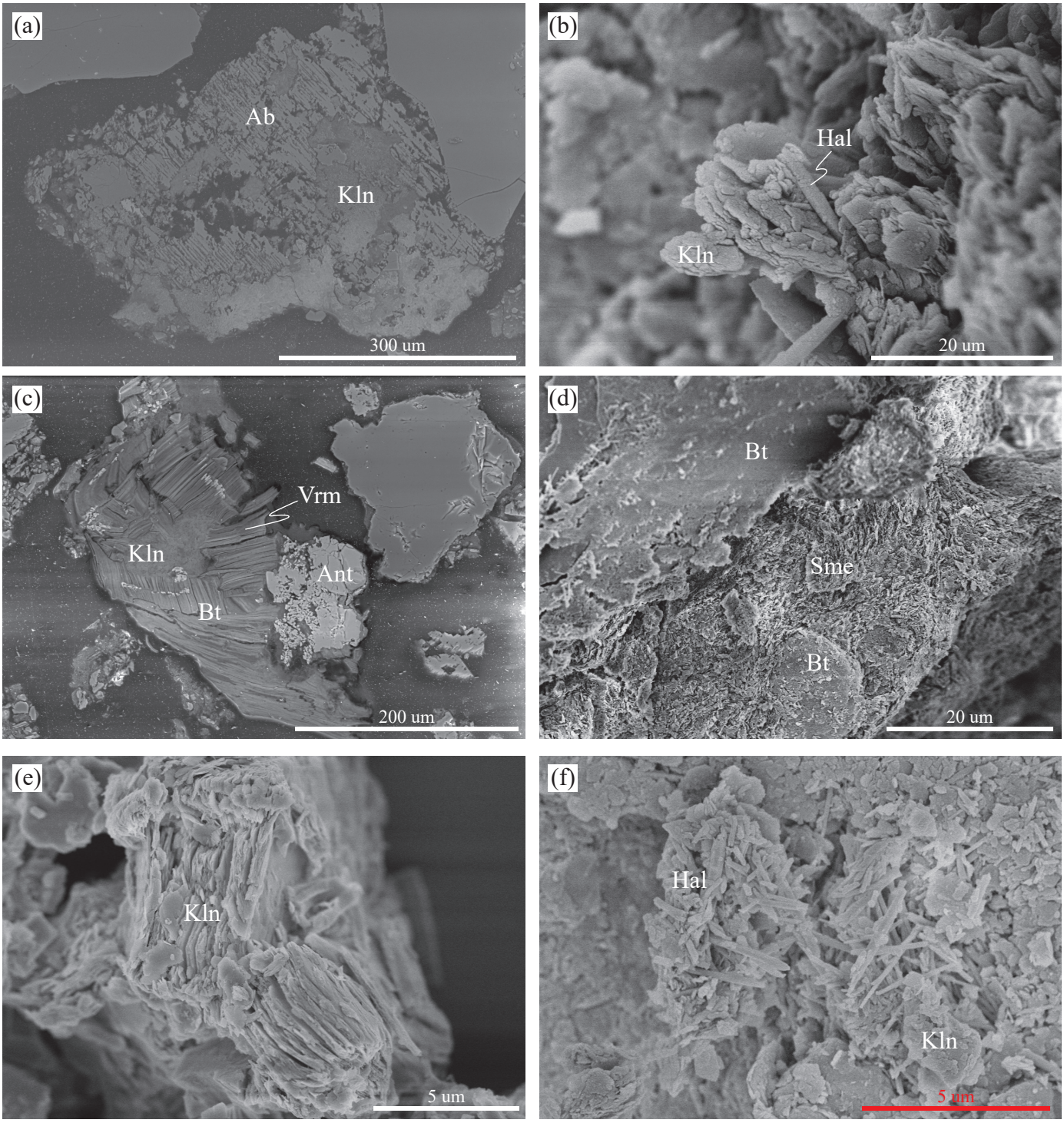

Figure 4

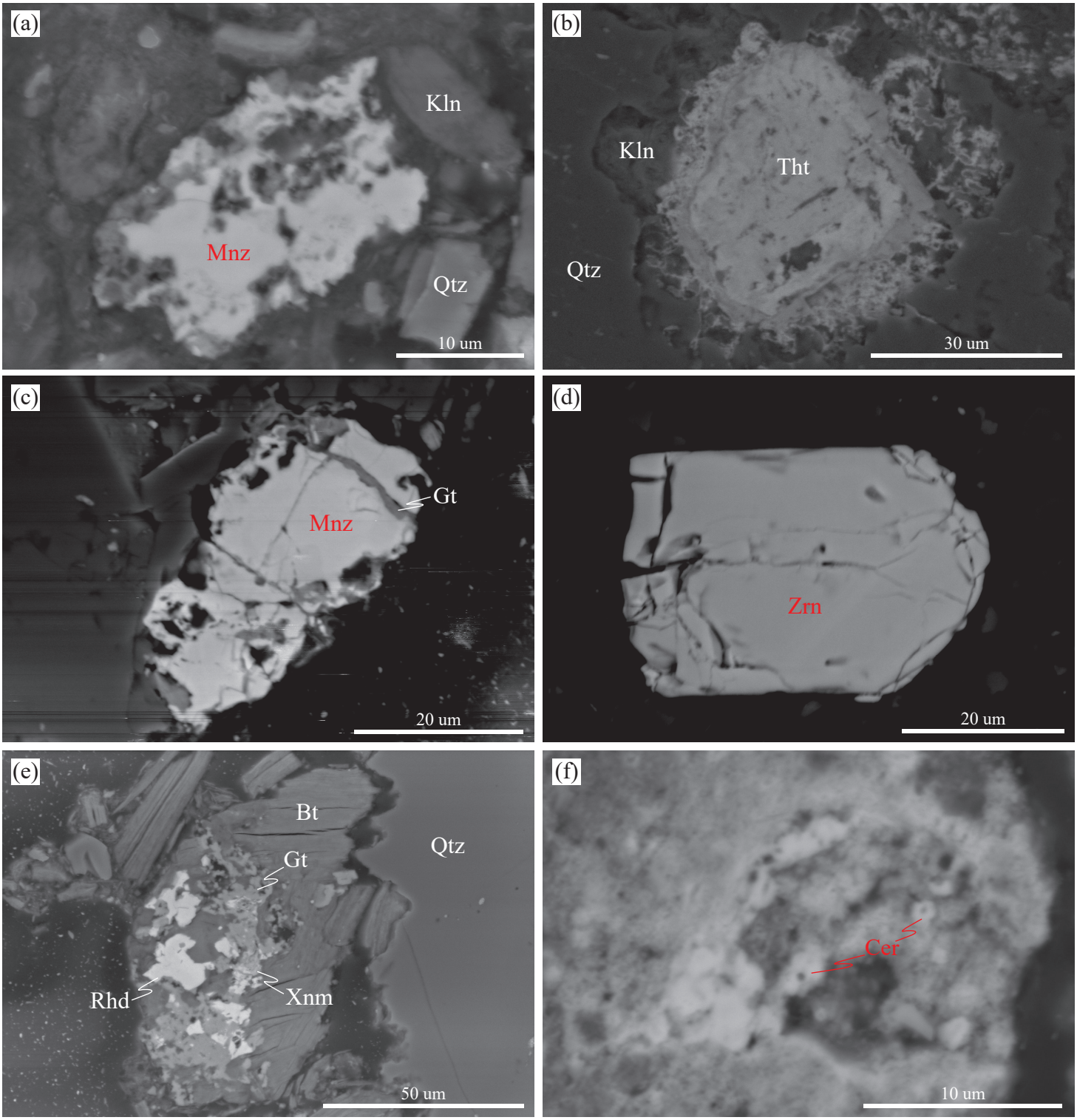

Figure 5

Li, M.Y.H., Zhou, M.-F., Williams-Jones, A.E., 2020. Controls on the Dynamics of Rare Earth Elements
During Subtropical Hillslope Processes and Formation of Regolith-Hosted Deposits. Economic Geology, 115(5): 1097-1118.

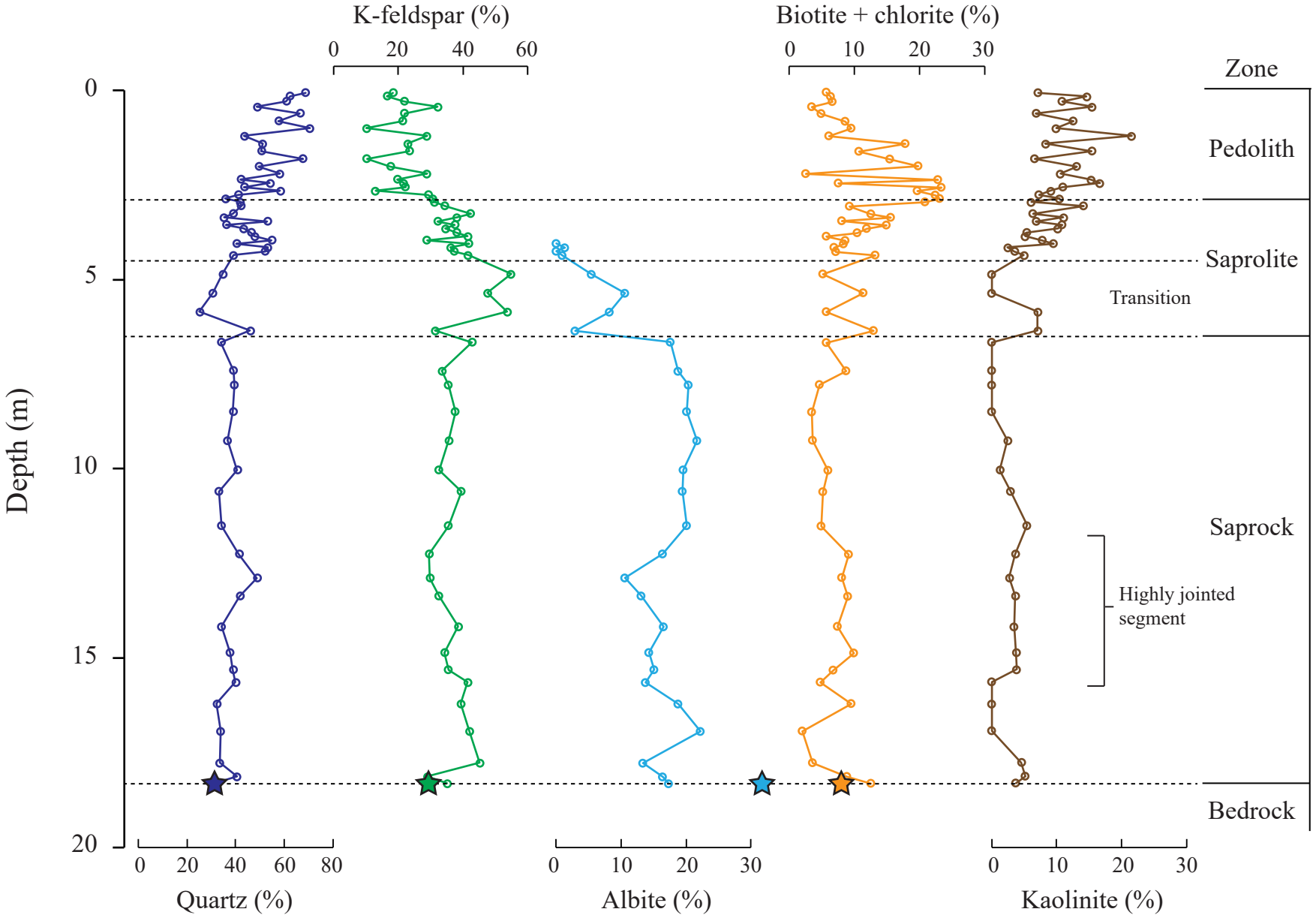

Figure 6

Li, M.Y.H., Zhou, M.-F., Williams-Jones, A.E., 2020. Controls on the Dynamics of Rare Earth Elements
During Subtropical Hillslope Processes and Formation of Regolith-Hosted Deposits. Economic Geology, 115(5): 1097-1118.

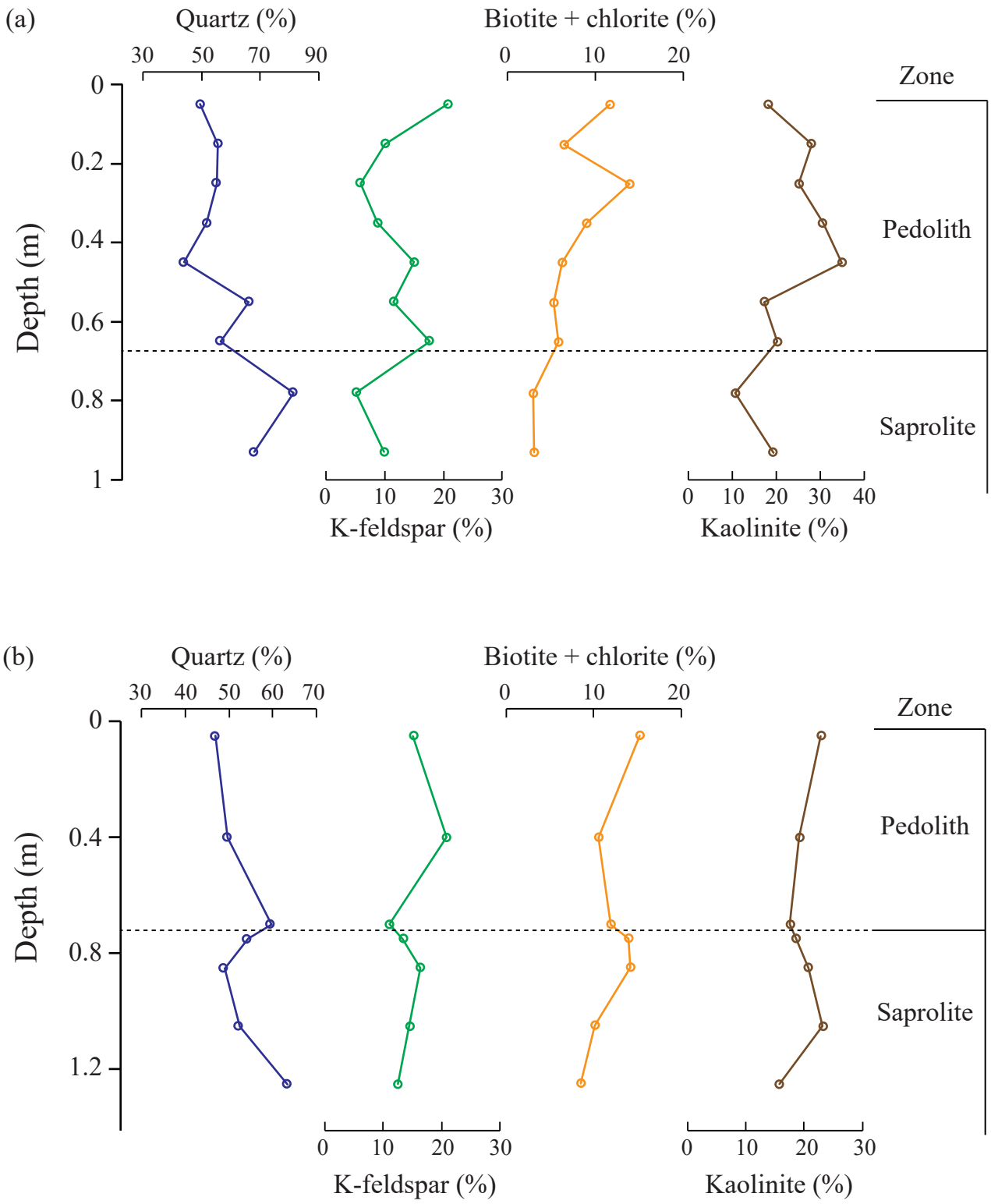

Figure 7

Li, M.Y.H., Zhou, M.-F., Williams-Jones, A.E., 2020. Controls on the Dynamics of Rare Earth Elements
During Subtropical Hillslope Processes and Formation of Regolith-Hosted Deposits. Economic Geology, 115(5): 1097-1118.

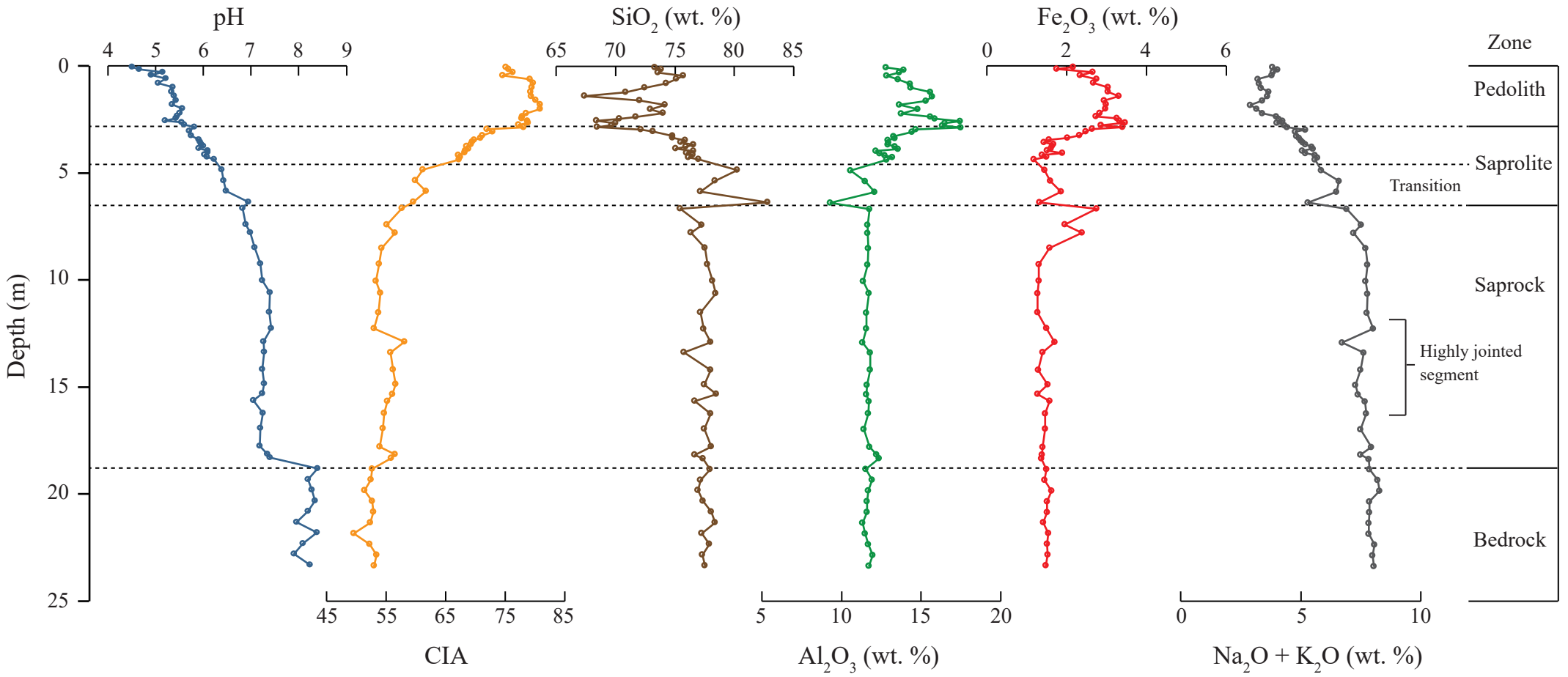

Figure 8

Li, M.Y.H., Zhou, M.-F., Williams-Jones, A.E., 2020. Controls on the Dynamics of Rare Earth Elements
During Subtropical Hillslope Processes and Formation of Regolith-Hosted Deposits. Economic Geology, 115(5): 1097-1118.

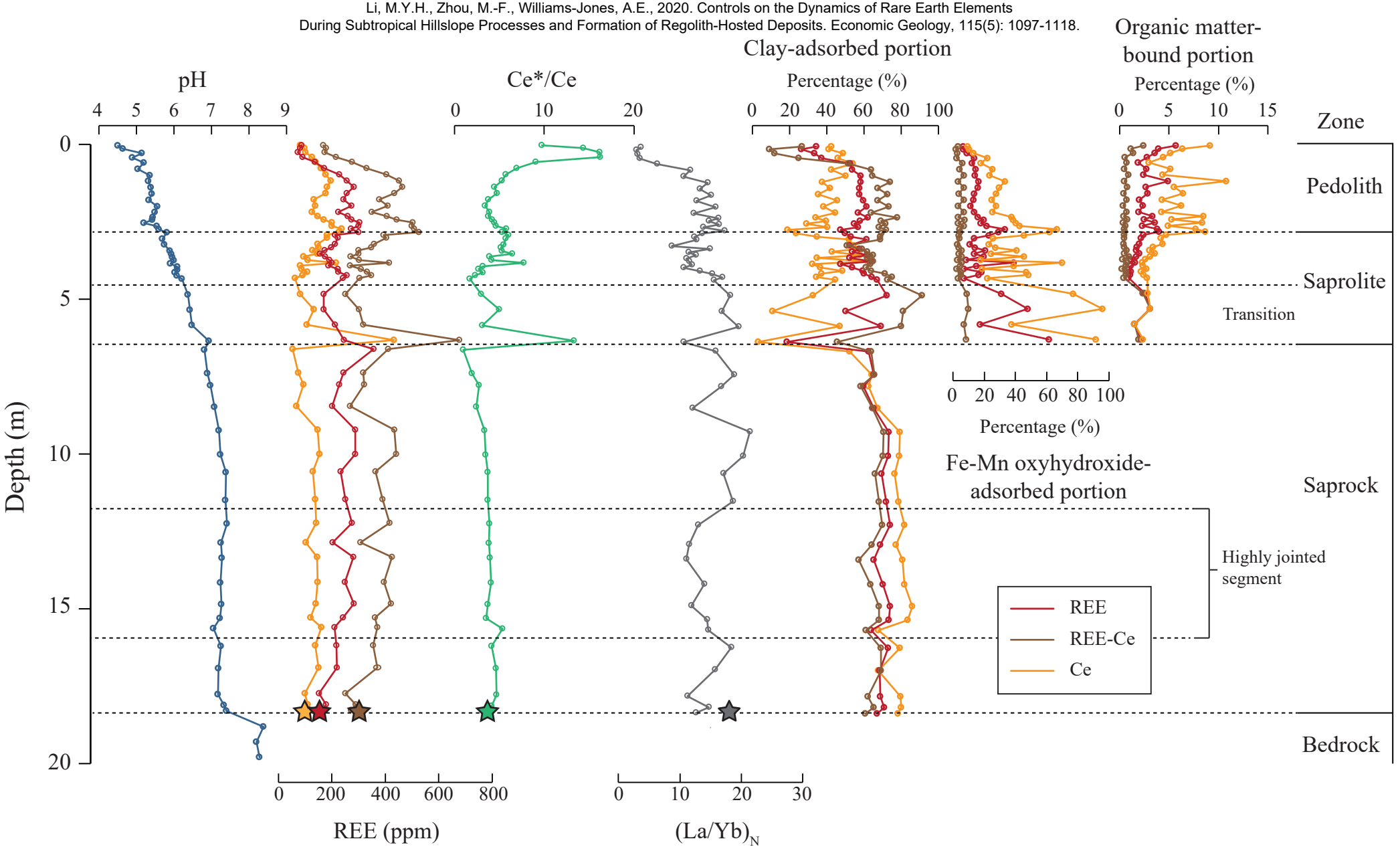

Figure 9

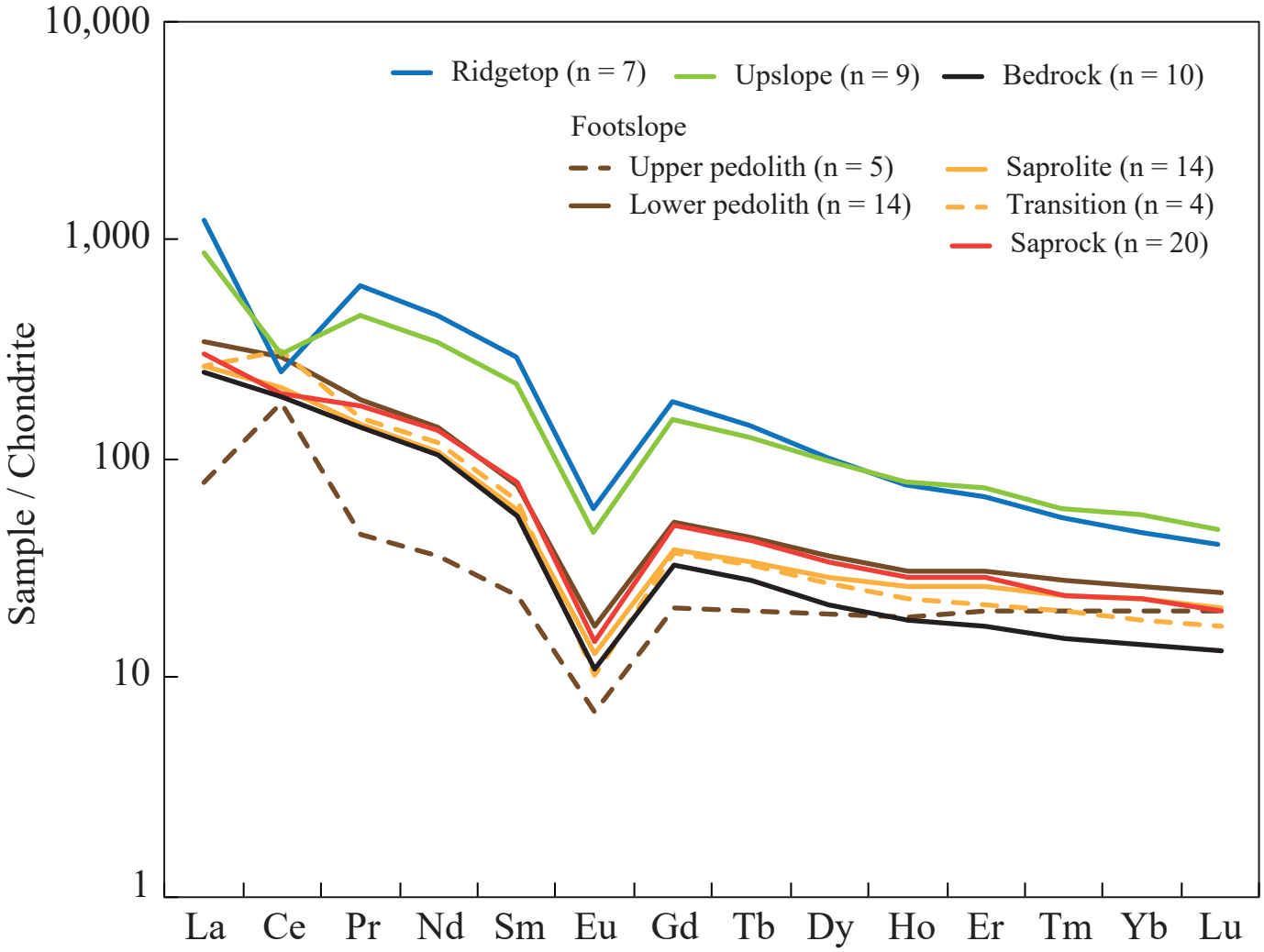

Figure 10

Li, M.Y.H., Zhou, M.-F., Williams-Jones, A.E., 2020. Controls on the Dynamics of Rare Earth Elements
During Subtropical Hillslope Processes and Formation of Regolith-Hosted Deposits. Economic Geology, 115(5): 1097-1118.

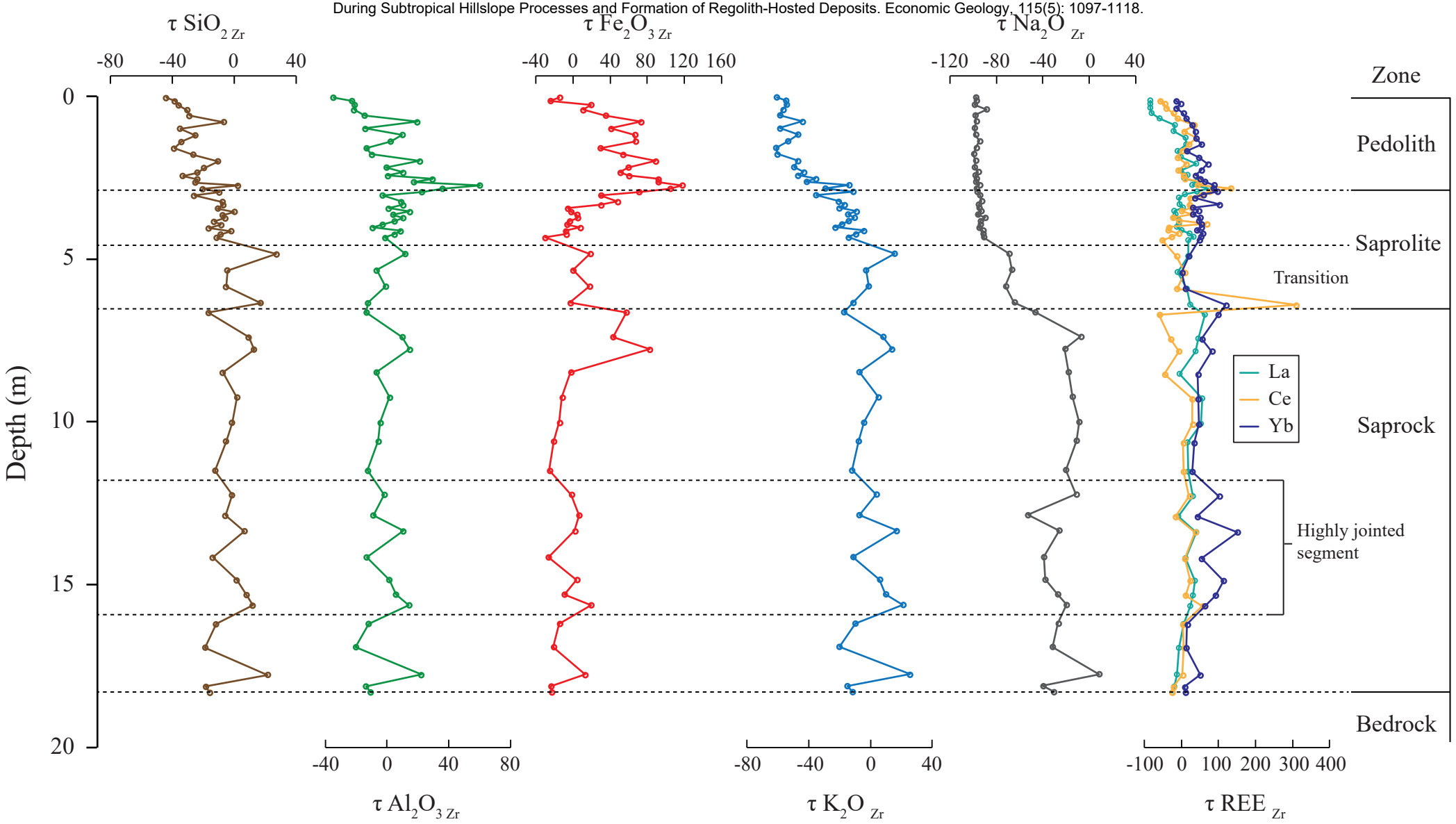

Figure 11

Li, M.Y.H., Zhou, M.-F., Williams-Jones, A.E., 2020. Controls on the Dynamics of Rare Earth Elements
During Subtropical Hillslope Processes and Formation of Regolith-Hosted Deposits. Economic Geology, 115(5): 1097-1118.

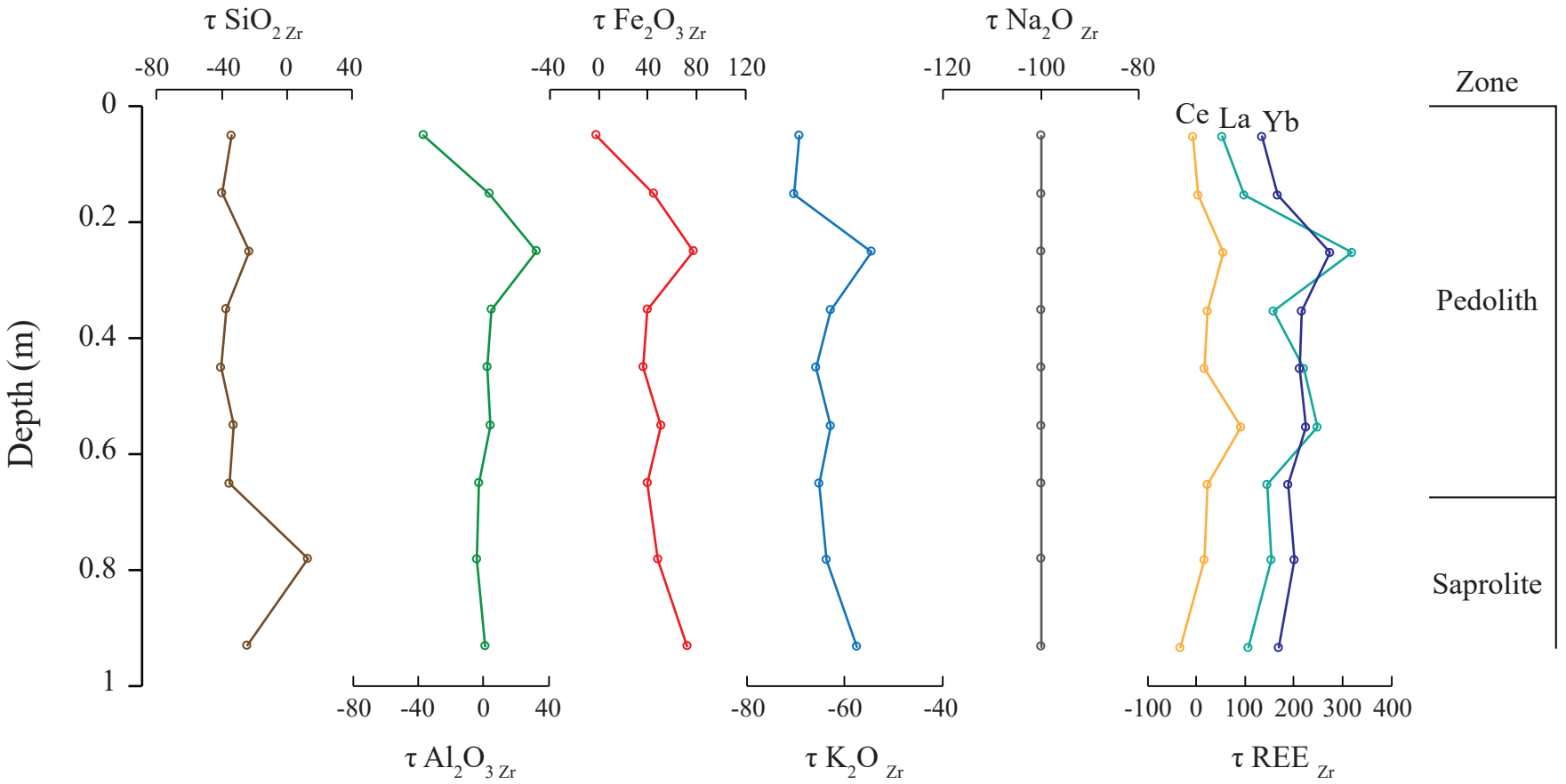

Figure 12

Li, M.Y.H., Zhou, M.-F., Williams-Jones, A.E., 2020. Controls on the Dynamics of Rare Earth Elements
During Subtropical Hillslope Processes and Formation of Regolith-Hosted Deposits. Economic Geology, 115(5): 1097-1118.

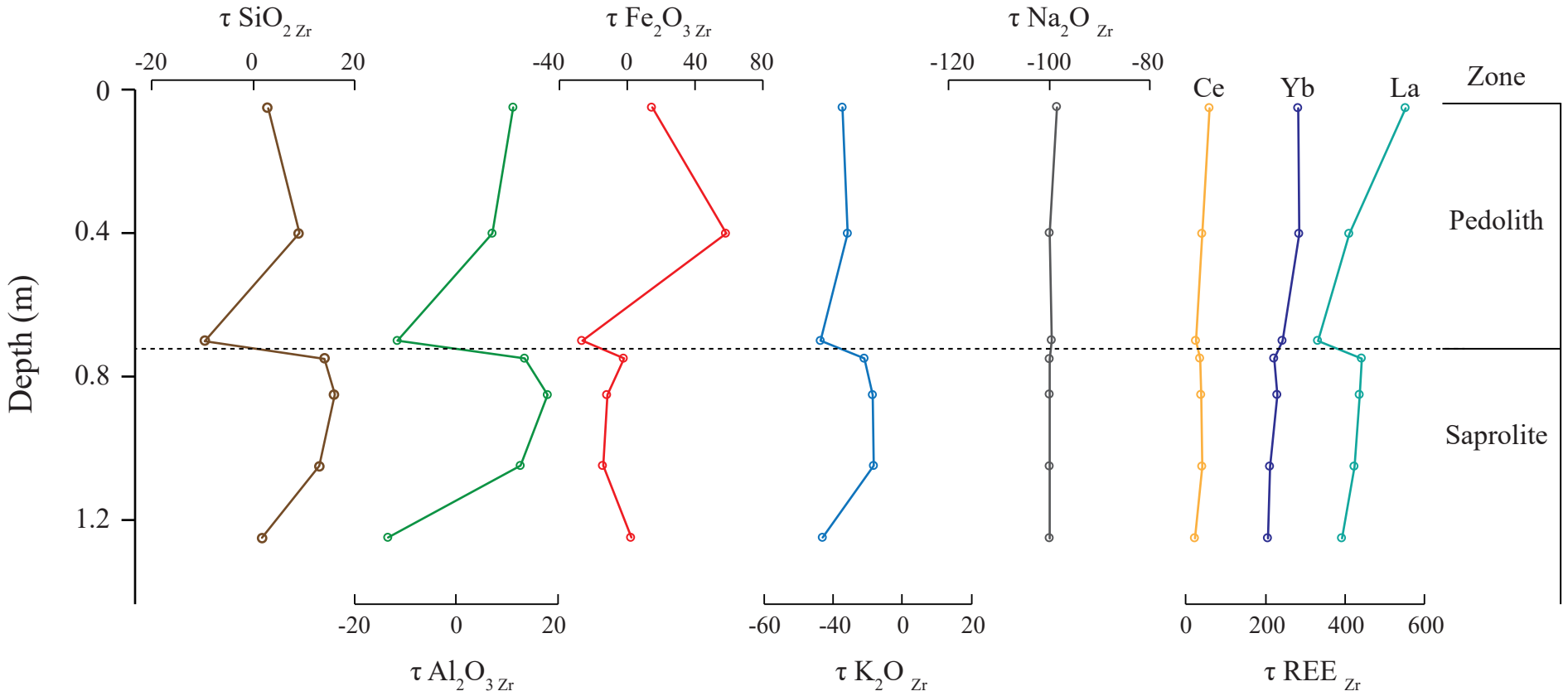

Figure 13

Li, M.Y.H., Zhou, M.-F., Williams-Jones, A.E., 2020. Controls on the Dynamics of Rare Earth Elements During Subtropical Hillslope Processes and Formation of Regolith-Hosted Deposits. Economic Geology, 115(5): 1097-1118.

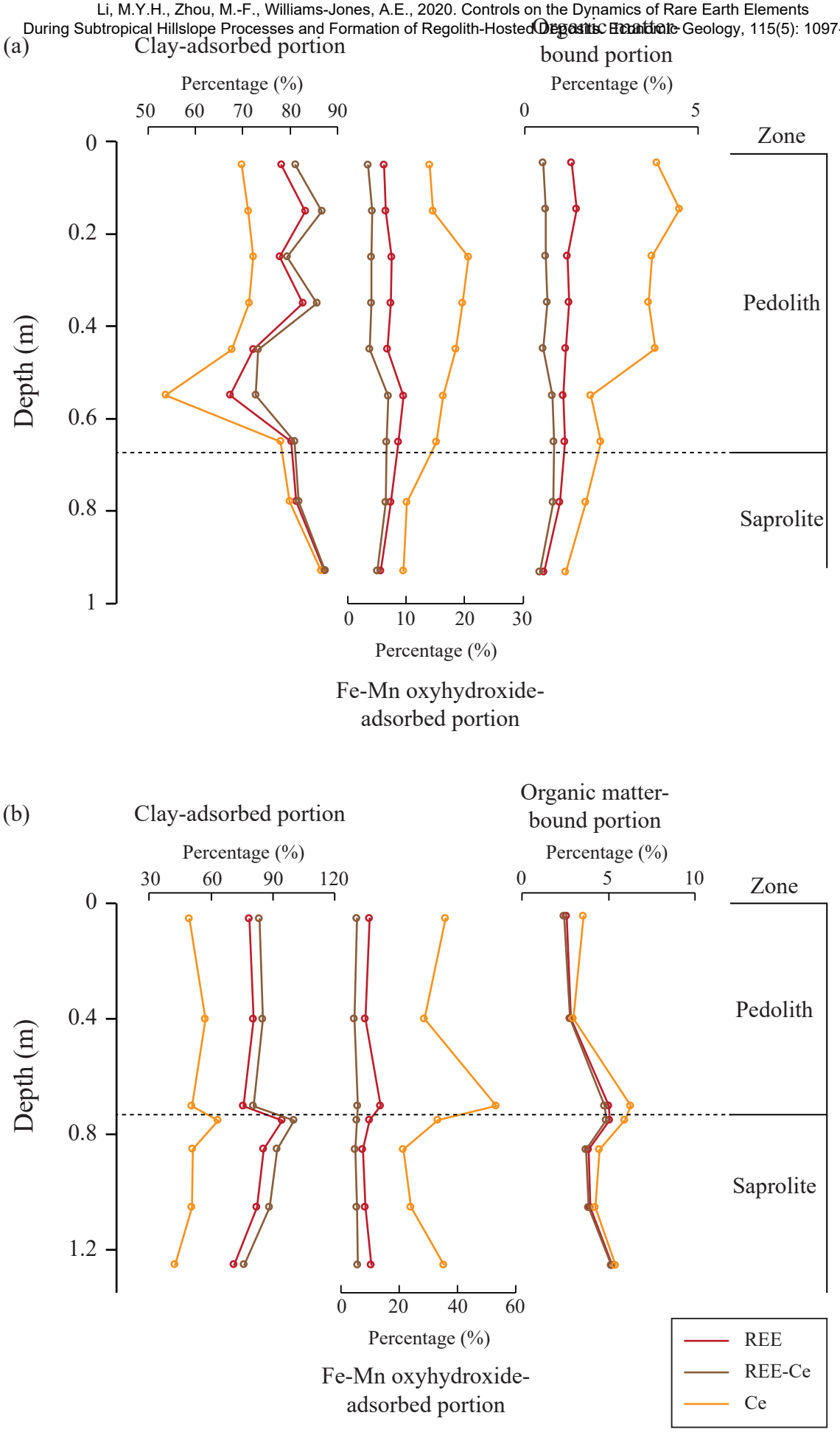

Figure 14

Li, M.Y.H., Zhou, M.-F., Williams-Jones, A.E., 2020. Controls on the Dynamics of Rare Earth Elements
During Subtropical Hillslope Processes and Formation of Regolith-Hosted Deposits. Economic Geology, 115(5): 1097-1118.

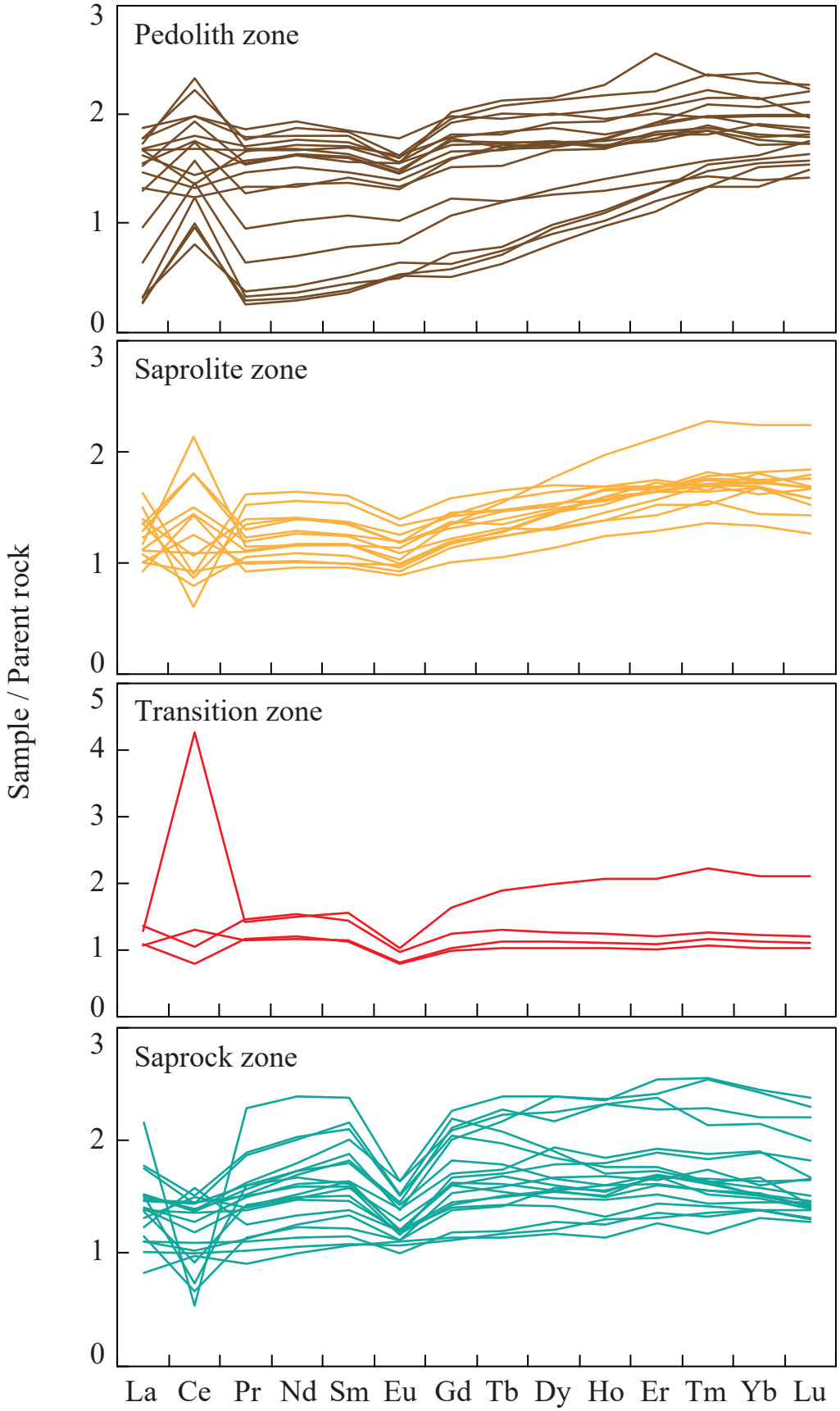

Figure 15

Li, M.Y.H., Zhou, M.-F., Williams-Jones, A.E., 2020. Controls on the Dynamics of Rare Earth Elements
During Subtropical Hillslope Processes and Formation of Regolith-Hosted Deposits. Economic Geology, 115(5): 1097-1118.

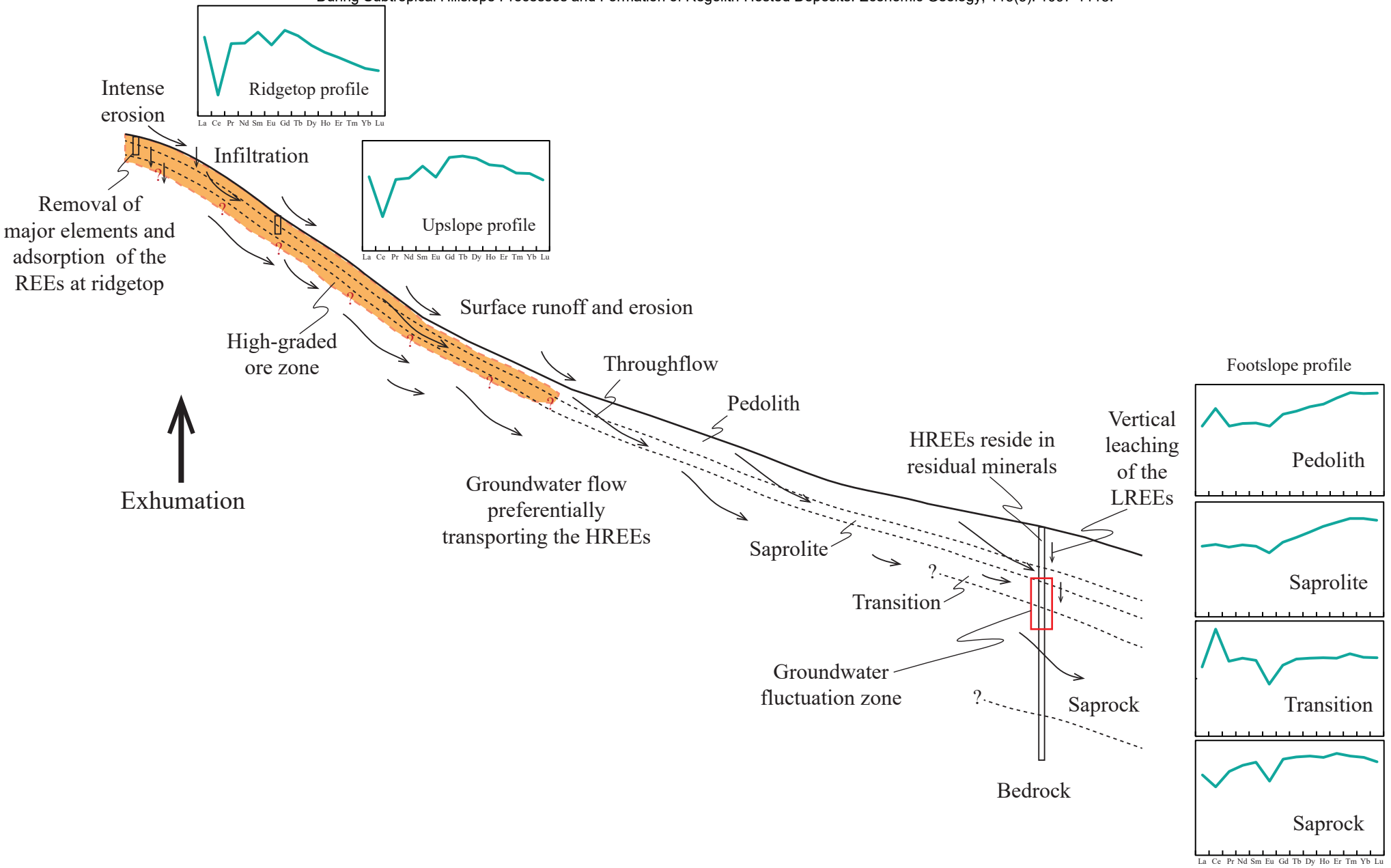

Figure 16

Table 1. Mass balance circulation results for different positions of the studied hillslope

	Parent granite	Ridgetop		Mid-slope			
W*	-	-0.049		1.48			
E*	-	3.05		1.52			
Q*	-	54.9		82.3			
CDF*	-	-0.02		0.5			
For individual elements							
	C	C	W*	CDF*	C	W*	CDF*	C
Major elements								
Si	36.2	36.9	-4.05	-0.04	33.9	66.5	0.61	33.8
Ti	0.10	0.13	-0.09	-0.31	0.16	-0.04	-0.14	0.20
Al	6.17	6.10	-0.10	-0.01	8.25	-0.58	-0.03	7.47
Fe	1.05	1.09	-0.19	-0.06	2.03	-2.81	-0.88	1.74
Mn	0.02	0.004	0.04	0.77	0.01	0.03	0.37	0.01
Mg	0.09	0.03	0.20	0.70	0.14	-0.29	-3.04	0.08
Ca	0.26	0.03	0.69	0.90	0.02	0.78	1.50	0.03
Na	1.00	0.00	2.99	1.00	0.0001	3.00	2.02	0.05
K	3.07	1.89	3.45	0.37	1.48	8.20	1.05	2.20
P	0.01	0.01	0.00	0.03	0.003	0.02	1.16	0.01
Trace elements								
Sc	3.58	4.30	-2.36	-0.22	7.75	-11.6	-1.00	8.14
Y	28.9	108	-243	-2.81	117	-120	-1.91	44.7
Nb	21.6	26.5	-16.1	-0.25	31.6	1.25	-0.01	28.6
La	58.3	285	-693	-3.96	205	108	-1.20	64.4
Ce	116	152	-117	-0.34	181	-18.1	-0.09	147
Pr	13.1	56.8	-134	-3.40	43.1	15.7	-1.06	14.0
Nd	47.6	204	-479	-3.36	156	50.5	-1.07	51.8
Sm	8.35	42.9	-106	-4.22	33.3	3.54	-1.61	9.43
Eu	0.63	3.31	-8.20	-4.31	2.63	-0.02	-1.75	0.80
Gd	6.68	37.5	-94.4	-4.72	30.8	-6.4	-2.13	8.71
Tb	1.02	5.30	-13.1	-4.28	4.70	-2.29	-2.17	1.36
Dy	5.43	25.6	-61.6	-3.78	24.8	-19.2	-2.20	7.77
Ho	1.02	4.45	-10.5	-3.41	4.39	-3.42	-2.00	1.54
Er	2.78	11.4	-26.4	-3.16	12.0	-11.8	-2.07	4.52
Tm	0.38	1.39	-3.11	-2.73	1.48	-1.4	-1.74	0.64
Yb	2.37	8.01	-17.3	-2.43	9.32	-11.1	-1.86	4.02
Lu	0.33	1.08	-2.28	-2.28	1.21	-1.26	-1.61	0.57
Hf	5.42	5.90	-1.74	-0.11	7.49	0.05	0.00	6.60
Ta	2.03	2.44	-1.36	-0.22	2.75	0.99	0.13	2.50
Th	28.0	38.0	-31.9	-0.38	45.5	-8.0	-0.13	40.4
U	7.32	6.82	1.16	0.05	7.86	6.83	0.32	5.02

Footslope
0.043
2.96
115
0.01

W*	CDF*
18.0	0.16
-0.29	-0.84
-0.37	-0.02
-1.09	-0.37
0.04	0.75
0.15	0.45
0.69	0.50
2.80	-257
2.24	0.08
-0.01	-0.78
-11.7	-0.99
77.3	-0.01
-7.23	-0.11
215	0.40
4.45	-0.02
46.1	0.43
163	0.41
36.0	0.40
2.55	0.28
30.3	0.25
4.49	0.22
21.4	0.13
3.28	0.05
7.58	-0.07
0.71	-0.14
4.37	-0.16
0.47	-0.18
-0.08	-0.01
-0.23	-0.04
-16.9	-0.21
12.8	0.57